Ruben Miguel Seixas Aguincha

Licenciatura em Ciências de Engenharia Física

Carbon Based Surfaces with Low Secondary Electron Emission

Dissertação para obtenção do Grau de
Mestre em Engenharia Física

Orientador: Nenad Bundaleski, Investigador, FCT-UNL

Co-orientador: Orlando Teodoro, Professor Associado, FCT-UNL

Júri:

Presidente:	Prof. Doutora Isabel Catarino
Arguente:	Prof. Doutor André Wemens
Vogal:	Doutor Nenad Bundaleski

FACULDADE DE
CIÊNCIAS E TECNOLOGIA
UNIVERSIDADE NOVA DE LISBOA

Setembro, 2018

Carbon Based Surfaces with Low Secondary Electron Emission

"Passion is what gets you through the hardest times that might otherwise make strong men weak, or make you give up."
Neil Degrasse Tyson

Acknowledgements

First of all I would like to thank to Faculdade de Ciências e Tecnologia of Universidade Nova de Lisboa (FCT-UNL) for being the great school it is, where I could learn, make friends and have unforgettable moments throughout these years.

I would also like to thank to the following people:

Nenad, for the first of many bus rides, where the idea for this same work came up; For the entire support, good mood, patience and being the greatest teacher in these past months.

Professor Orlando, for agreeing to be my co-supervisor and for all the patience and teachings, not only in these past few months but throughout the entire course.

Ana and Afonso, for all the support, ideas, help and good will.

Paulo Duarte from REQUIMTE, for the help in my introduction to electrochemistry.

The research team of Plasma Engineering Laboratory at Institute of Plasma and Nulcear Fusion of IST and particularly Neli Bundaleska, for providing graphene/N-graphene samples produced in the framework of PEGASUS (H2020 FETOPEN 766894) project. Without it, my entire work wouldn't be possible.

All my family and friends, for the incredible patience, support and everlasting friendship.

My parents, for their greatest effort so I could get to this very moment.

My "fatty" sis for being the greatest sister, friend and role model I could ever ask for.

Last but not least, a very special thank you Carolina, for all the support, patience and love through all these years.

ABSTRACT

Low secondary electron emission materials have significant impact in accelerator and space technologies. Secondary electrons produced by the residual gas ionization or due to the irradiation of chamber walls by the synchrotron light influence trajectories of charged particles inside accelerators. Significant potential difference between the dielectric and conductive parts of satellites is caused by different secondary electron emission yields induced by cosmic rays, leading to discharges between different parts of a satellite, resulting in the malfunctioning of the communication systems and other sensitive equipment. One of the solutions to these problems is coating surfaces with thin films of amorphous carbon. Recent studies showed that graphene-based coatings have a potential in further reduction of secondary electron yields (SEY). For that reason, the deposition of free standing graphene (i.e. graphene in the form of powder) on technical surfaces of interest in space and accelerator technologies using Electrophoretic Deposition (EPD) was investigated in this work. Highly oriented pyrolytic graphite and pure graphene samples were used as references in order to compare them with graphene coatings produced by EPD. Apart from SEY measurements, X-ray photoelectron spectroscopy and scanning electron microscopy of the samples were performed for that purpose. Graphene depositions were successfully made and the maximum SEY of technical surfaces (stainless steel and copper) was reduced to $\sim$1. In order to achieve these results, various studies were performed concerning the deposition technique parameters, related to the process and the materials used. Three different alternatives were also explored.

Keywords: Accelerator, Satellite, SEY, Graphene, EPD, XPS, SEM.

RESUMO

Materiais com baixa emissão secundária de electrões têm um grande impacto na tecnologia espacial e de aceleradores de partículas. A trajectória das partículas carregadas no interior dos aceleradores é influenciada por electrões secundários produzidos pela ionização de gás residual ou pela irradiação das paredes das câmaras por radiação de sincrotrão. Nos satélites de comunicações, a radiação cósmica origina diferentes taxas de emissão de electrões secundários em materiais condutores e dielétricos constituintes do equipamento. Este efeito origina grandes diferenças de potencial entre estes materiais, consequentemente levando à avaria e mau funcionamento dos sistemas de comunicações e outros equipamentos sensíveis. Uma das soluções para estes problemas é revestir as superfícies com filmes finos de carbono amorfo. Estudos recentes demonstram que revestimentos à base de grafeno têm um grande potencial na redução da taxa de emissão de electrões secundários (SEY). Por esta razão, foi estudada neste trabalho a deposição electroforética (EPD) de grafeno em forma de pó em superfícies técnicas no interesse da tecnologia espacial e de aceleradores de partículas. Grafite pirolítica altamente orientada e grafeno puro (na forma de pó) foram usados como referências com o objectivo de poderem ser comparadas às deposições de grafeno produzidas por EPD. Além de medições de SEY, XPS e SEM foram também usadas para analisar e caracterizar as amostras produzidas. As deposições de grafeno foram realizadas com sucesso e foi ainda possível diminuir o SEY das superfícies técnicas usadas (aço inoxidável e cobre) para $\sim$1. Para atingir os resultados obtidos, foram realizados vários estudos relativamente aos parâmetros do processo de deposição e aos materiais usados na mesma. Foram ainda exploradas três diferentes alternativas a este processo.

Palavras-chave: Aceleradores de partículas, satélites de comunicações, SEY, Grafeno, EPD, XPS, SEM.

Contents

List of Figures

List of Tables

CHAPTER 1

INTRODUCTION

Development of low Secondary Electron Yield (SEY) materials is very important in different modern technologies, spanning from space applications, via modern accelerators, to the vacuum gauges. Altering the surface composition with coatings of amorphous carbon to reduce SEY has been studied for years. This resulted in recent coating of several kilometers of tubes by this material in Super Proton Synchrotron in CERN, which is the accelerating device preceding Large Hadron Collider [1]. Recent investigations have shown that this could be further improved with graphene coatings [2]. Since graphene is a form of graphitic carbon it has low secondary electron emission and its unusual properties let us suppress the SEY even further [3]. It is important to point out that not every kind of carbon has low SEY, only the conductive ones. Graphene, the first 2D material discovered by Geim and Novoselov in 2004, is conductive carbon material with numerous interesting properties including low SEY. Graphene can be produced by a great variety of methods but each of them will result in different types of graphene, concerning its defects and impurities, which will influence its secondary emission properties.

The main goal of this project will be to study SEY from carbon coatings, and correlate the surface characteristics (composition, morphology and electronic structure) with the secondary electron emission properties. It will be used an electrochemical technique (Electrophoretic Deposition - EPD) to produce different coatings, and to further study the influence of substrates and different deposition parameters. The composition of surfaces will be characterized by XPS and its morphology by SEM, while the SEY will be measured on the existing home-made apparatus [4].

This project has been developed within CEFITEC (Centro de Física e Investigação Tecnológica) in Surface Science and Vacuum Technology Lab in collaboration with IPFN (Instituto de Plasmas e Fusão Nuclear) from IST (Instituto Superior Técnico) and INL (International Iberian Nanotechnology Laboratory) for the production of the graphene.

1.1 State of the Art

Secondary electron emission (SEE) has always been a problem in particle accelerators and in space technologies, namely, communications satellites. The problem known as electron cloud (e-cloud) was discovered by Soviet accelerator scientists from Novosibirsk the middle 60-ies. But, at that time, it was of minor significance with respect to other problems related to the beam stability. With the advancement of the accelerator technologies e-cloud effect became the major limitation of modern accelerators and synchrotrons.

Everything begins with the ionisation of the residual gas. As a result of that, one energetic electron is kicked out from the atom/molecule hitting the tube wall and may initiate electron multiplication. Electron cloud is formed, which will live for some time before being absorbed. In accelerators, ions travel in the form of bunches (pulses). If an electron cloud survives until the next bunch come to the same spot, negative charges will bend the beam and introduce the instability. If the objective is to increase the number of collisions in the accelerator, the number of bunches per second needs to be increased (i.e. decrease the time between bunches). For that reason, the lifetime of an e-cloud must be reduced.

Low energy electrons have low SEY because the probability to originate secondary electrons is also low, but for electrons at energies and angles with secondary electron yield above 1, the number of secondary electrons grows exponentially [5]. These electrons will interfere with the primary beam which may influence its trajectory and cause beam instabilities.

Concerning telecommunication satellites, SEE influences the maximum power handling capabilities of the satellite waveguide components. The Multipactor effect is an electron cloud in devices working in vacuum, where the exponential electron multiplication by SEE from the walls in resonance with the radio frequency field, distorts the signal and eventually evolves into discharge between the dielectric and conductor materials damaging and even destroying the communications devices [6].

Nowadays there are three main solutions to this subject [7]:

1. Changing the surface composition;
2. Modifying the surface morphology;
3. The “Dose” effect.

Regarding accelerator components or vacuum chambers all three approaches are being applied, particularly the first and the third. Although changing the surface morphology is a complex method to apply in a large scale, CERN recently invested in a laser mechanism to create grooves along the tubes. The third method will also be explained further but this report will be focused mainly on the first and second since they are the ones that are going

to be employed.

Changing the surface composition has been the solution under numerous investigations, since it is the most suited method concerning its application in this area of interest. Ideally clean metals are much better for this purpose but they lead to other problems, namely, the oxidation of their surface which alters completely their properties. So, this method consists in applying a thin film of another material on a certain surface. This material must have very good SEE properties which leads to low SEY, and they must be chemically inert, so the properties of the film material are one of the main concerns of this method. Throughout the years there has been various studied materials which led to a reduction of the SEY, such as TiN, TiC, NbC and NbN. Titanium Nitride (TiN) films are known to reduce SEY [8] depending on the deposition method. From various studies there is a large variation of results concerning maximum SEY measurements, but the best layers of TiN are known to have maximum SEY values (1.6 - 1.7) lower than any known as-received metals (2.5 - 3) [9][7]. All other materials have revealed very similar results for the minimization of the multipacting effect although their exposure to air resulted in an increasing of the SEY ($\sim$ 0.4 for TiN) [10]. It is essential to preserve low SEY after air exposure and after baking, since these are potential walls of UHV chambers, which will be opened or baked, from time to time. In that respect, TiN would not be a suitable choice.

In the last few years, coatings of amorphous carbon, graphite and more recently graphene, have been frequently studied because of their SEE properties. Amorphous carbon and graphite are two forms of carbon with the lowest known SEY's in the literature (1 - 1.5) [11]. Amorphous carbon is a reactive allotrope of carbon that does not have a crystalline structure and is usually stabilized with hydrogen bonds in terminating free π bonds. Carbon coatings prepared by magnetron sputtering can reach a maximum SEY close to 1 with a deviation that can go from 0.8 to 1.15 depending on their aging process (increasing the amount of hydrogen due to air exposure) [11]. Graphene is a very special material due to its unique electronic, optical, mechanical and thermal properties. Studies have showed that a mono/double layer of graphene on a flat substrate in vacuum has ultralow SEY, of the order of 0.5 [6]. The graphene can be synthesized by a variety of methods and in some cases, it can be grown directly on the substrate (Au, Ag, Cu and Si) which make it even easier to be used as a low SEY material. It was shown in different studies that graphene coatings, chemically made from graphite, can reduce the SEY of the surface at least 50% with the thickness of the film in a nano-scale [12].

A second method to suppress the SEY of a surface is changing its surface morphology. When secondary electrons are produced due to the collision of primary electrons with the surface, according to the emission angle, some can escape the grooves while the rest hit the inner side of the groove. With some probability they will be absorbed or generate second generation secondary electrons. This process may repeat itself until the energy

of future generations secondaries is low enough that they are absorbed by the surface [13]. The corrugations can be produced by electrochemical reactions directly with the substrate (so called chemical etching) or by the deposition of strongly roughened layer. This method was first tested in a copper substrate [7], where it was grown an oxide layer at high temperatures and the stress generated by the sudden temperature change, led to the opening of cracks in the oxide layer which created specific surface morphology [7]. This oxide layer (as any metallic oxide) has a relatively high SEY, so when combined with surface roughness it can be clearly seen a suppression in SEE. Altering the surface morphology is an efficient way to reduce the SEY but it's a difficult method to apply to a larger scale.

A combination of the first and second methods can also be possible when it is used amorphous carbon or free-standing graphene coatings [6] where the SEE properties of the material are extremely good but its roughness decreases even more the SEY.

Finally, there is a third solution to this secondary electron emission yield subject known as the "Dose" effect. This process consists in the SEY reduction by the electron bombardment of the surface. This method is studied correlating SEY values with electron doses. It is proved that SEY decreases with applied electron doses [7]. There are also studies that investigate the dose effect in different components of the total SEY such as its angular dependence with the primary electron beam [14].

CHAPTER 2

CONCEPTS AND EXPERIMENTAL TECHNIQUES

In this section, it will be explained all the important fundamental concepts and the different techniques used in this work. Being so, this chapter is divided into two main parts, the theoretical concepts and the experimental techniques.

2.1 Fundamental Concepts

2.1.1 Secondary Electron Emission - SEE

When an electron hits a material, there is electron emission from the material itself. This process is called secondary electron emission (SEE) and can be divided into three main steps (Figure 2.1):

1. A primary electron collides and gets into the sample. While inside the material this primary electron excites other electrons loosing energy in this process. The excited electrons with enough energy to leave the surface are secondary electrons.

2. The secondary electrons created in step 1 will be interacting with the material and loosing the energy until they reach the surface. The main mechanism of energy loss is via excitation of valence band electrons. In that respect, the most efficient energy loss is achieved in conductive materials that do not have energy barrier for the electron excitation.

3. Finally, once they reach the surface a fraction of the secondary electrons will be able to escape. Some electrons will have kinetic energy above the work function and still be reflected back to the material: they need to have enough momentum normal to the surface. And even if they have enough momentum normal to the surface, they can still be backscattered, due to the quantum effects.

These previous steps only explain the origin of the true secondary electrons, the ones originated inside the material and with kinetic energy below 50 eV. But, when an electron beam is focused on a surface, some of those electrons can be elastically reflected while the rest of them get through the material. Some of these are inelastically reflected out of the material after losing some energy, and since their trajectory is usually close to the surface, these will be responsible for producing secondary electrons close to it by the energy transfer. The remaining electrons will be responsible for the true secondary electrons by diffusion and absorption processes.

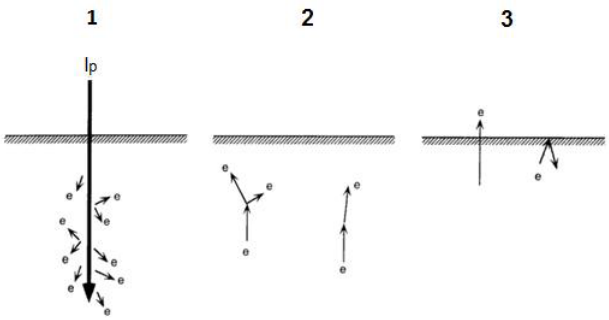

Figure 2.1: Three steps for the productions of true secondary electrons [4].

2.1.2 Secondary Electron Yield - SEY

It is important to stress that all electrons emitted from the surface i.e. true secondary, inelastically and elastically backscattered electrons contribute to the formation of an electron cloud, and should be therefore suppressed. It is therefore of interest to measure the yield of all these electrons, which is sometimes denoted as total electron yield. However, the majority of emitted electrons have low energy and belong to the group of true secondaries. It is therefore common in the literature to denote the appropriate coefficient secondary electron yield although total electron yield is actually measured. Therefore the secondary electron yield (SEY), δ, is here defined as the number of emitted electrons per incident electron [2]. In practical terms, SEY is a ratio between the current generated by emitted electrons from the surface (I_e) and the current created by the primary electrons (I_p):

$$\delta = \frac{I_e}{I_p} \tag{2.1}$$

SEY as a function of primary electron energy can be described with its maximum value δ^m and corresponding primary electron energy which lies in the range between 200 and 400 eV for materials such as copper, aluminum and stainless steel. SEY of a material depends on the atomic number, surface chemistry, topography and the work function of the material [4].

2.1.2.1 Semi-empirical law for the emission of secondary electrons

Semi-empirical law describes the shape of the energy dependence of the yield of true secondary electrons. Since the energy dependence of the backscattered electrons (with kinetic energies above 50 eV) does not strongly depend on the primary electron energy, this expression also represents very good description of the energy dependence of all emitted electrons (i.e. total electron yield). Secondary electron yield, $\delta(E_p)$, depends on the rate at which secondary electrons are created as a function of the depth inside the material, $n(z, E)$ [15].

$$n(z, E) = -\frac{1}{\epsilon}\frac{dE}{ds} \tag{2.2}$$

where s stands for the path length of the electron along its trajectory, dE/ds is the stopping power (electron's energy transfer rate for its surrounding material) and ϵ is the necessary energy to create a secondary electron.

The probability that a secondary electron created at depth z will be emitted is usually considered to be

$$p(z) = Ke^{-\frac{z}{\lambda}} \tag{2.3}$$

where $K = 0.5$ assuming that the electrons are dispersed symmetrically inside the material, and λ is the effective escape depth of the secondary electron. This way:

$$\delta(E_p) = \int n(z, E)p(z)dz \tag{2.4}$$

The simplest way to model the curve of δ as a function of E_p is to assume that the stopping power is constant and all electron trajectories are straight and identical:

$$-\frac{dE}{ds} = \frac{E_{PE}}{R} \tag{2.5}$$

where R is the penetration depth of the incident electron. This way, δ can be rewritten by solving the integral (2.4)

$$\delta = 0,5\frac{E_{PE}}{\epsilon}\frac{\lambda}{R}(1 - e^{-\frac{R}{\lambda}}) \tag{2.6}$$

with R defined as a function of the primary energy:

$$R = \frac{B}{\rho}(E_p)^n \tag{2.7}$$

In this equation, $n = 1.67$ according to Lane and Zaffarano, $B = 76$ nm and E_p is in kilo electron volt (keV). ρ is the density of the material (g/cm^3) [15]. At the maximum, where $\delta = \delta^m$,

$$\frac{R}{\lambda} = \left(1 - \frac{1}{n}\right)(e^{\frac{R}{\lambda}} - 1) \tag{2.8}$$

and so, for $n = 1.67$, the last equation can be numerically solved, which gives $R = 1.614\lambda$. Combining this R value with (2.7) it is possible to get the energy, E_p^m at which δ is maximum (δ^m):

$$E_p^m \approx 1,33 \left(\frac{\rho\lambda}{B}\right)^{0,60} \tag{2.9}$$

Using this same energy in (2.6), then

$$\delta^m \approx \frac{0,33}{\epsilon} \left(\frac{\rho\lambda}{B}\right)^{0,60} \tag{2.10}$$

It has been proven that δ^m / E_p^m is a characteristic constant of the material. Combining a few of the previous equations, it is possible to eliminate ϵ and λ which are usually unknown parameters. This way, we end up with δ/δ^m in function of E_p/E_p^m which is material independent [15]:

$$\frac{\delta}{\delta^m} = 1,28 \left(\frac{E_p}{E_p^m}\right)^{-0,67} \left(1 - e^{-1,614\left(\frac{E_p}{E_p^m}\right)^{1,67}}\right) \tag{2.11}$$

This last result is known as "the universal law of secondary electron yield" which provides a conventional description of the phenomenon. Practically, it expresses the shape of the SEY curve which matches very well with the experimental results in the case of flat surfaces (Figure 2.2).

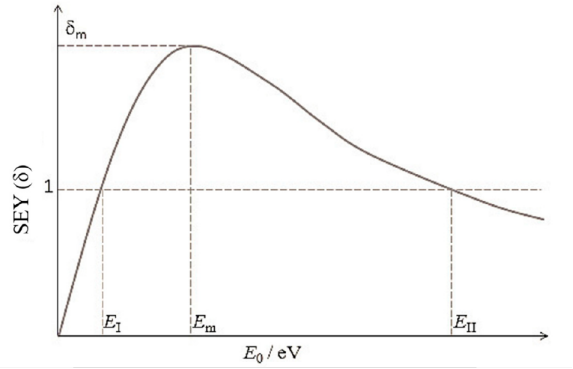

Figure 2.2: Illustration of a typical SEY curve as a function of primary electron energy [16].

2.1.2.2 Factors that may influence SEY

The electronic structure of a material is an important factor related to secondary electron emission. The electrons loose energy by exciting valence band electrons. When there is a gap between conduction and valence band, their excitation is suppressed so that the energy loss of secondary electrons is much slower. In other words, the effective escape depth from the expression 2.3, λ, is longer and the electrons may reach the surface even if they come from deeper layers. The secondaries can travel a lot without loosing the

energy. The larger the gap, the longer will be λ. If the objective is to reduce SEY, a small λ is needed so that the secondaries efficiently loose the energy.

Apart from the electronic structure of the material, there are two main factors that strongly influence the SEY: the incidence angle of the primary beam with the surface (this angle is measured with respect to the normal of the surface) and the surface roughness.

If the primary beam collides normally to the surface we consider its traveling depth to be x. Considering a different angle of incidence θ, the traveling depth of the primary electron is still x but the point at which the electron stopped from the surface is $xcos(\theta)$ (Figure 2.3). This new distance is shorter, and since secondary electrons are created closer to the surface, the probability of their emission increases according to the expression 2.3, leading to higher SEYs.

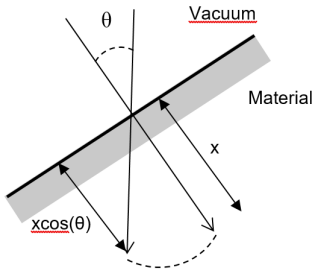

Figure 2.3: Correlation between the angle of incidence of primary electrons and their depth.

The other important factor is the roughness of the surface. In a smooth surface, an electron leaving the substrate has no obstacles at all, but in a roughened surface that does not happen. In that case, an electron leaving the surface has high probability to be recaptured by the protrusions (Figure 2.4). This effect leads to fewer ejected electrons from the surface which results in a lower SEY. Nevertheless, it is important to note that rough surface also implies oblique incidence of electrons to the sample, which may also increase SEY. Therefore, depending on the details of the surface topography, rough surface may both increase or decrease SEY.

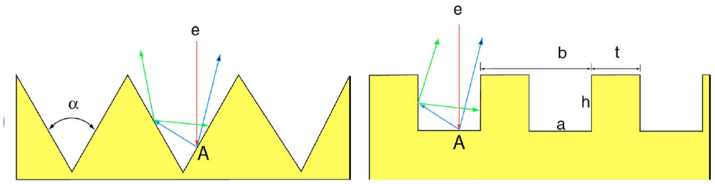

Figure 2.4: Examples for SEE on grooved surfaces [13].

Surface contamination may also increase SEY. As already referred, different materials have different SEE properties. In that sense, if a certain surface is contaminated with other

kind of materials or with even its own oxide (looking at the oxide as a contaminant), the secondary electron emission properties of the material will be influenced leading to an increasing of its SEY.

2.1.3 Graphene

Graphene is a two dimensional allotrope of carbon consisting of a single layer of carbon atoms arranged in a hexagonal lattice of graphite (Figure 2.5). Layers of graphene stacked on top of each other form graphite. It is the thinnest known compound with only one atom thick as well the lightest and the strongest compound discovered [17]. Graphene has unique electronic, mechanical, optical and thermal properties, among others, which makes it suitable to a very wide range of applications.

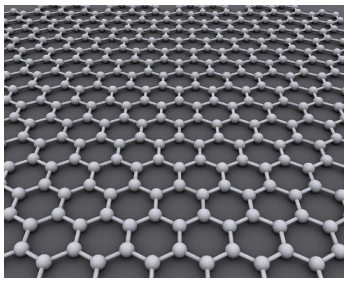

Figure 2.5: Hexagonal lattice of graphene.

2.1.3.1 Carbon Hybridization

Hybridization of atomic orbitals occur when atoms get ready to form bonds. It is when s and p orbitals merge together in order to create new lower energy sp orbitals. s and p orbitals combine with each others and allow an overlapping of the orbitals forming hybrid orbitals. Two different atoms having the same hybrid orbitals, come together resulting in an overlapping of these orbitals and a formation of a covalent bond.

There are three types of carbon hybridization (sp^1, sp^2 and sp^3) but only two will be explained since these are the ones that will be observed.

- sp^3 **Hybridization**

  Carbon atoms have the following electron configuration: $1s^2 2s^2 2p^2$. So, there are only two p orbitals that have unpaired electrons. For carbon being able to form such molecules as CH_4 (methane) or even a diamond structure, four equivalent bonding orbitals need to be created. This happens naturally when mixing one s orbital with the three p orbitals, producing four hybrid orbitals called sp^3 orbitals.

$$1s^2\ 2s^2\ 2p^2 \quad \longrightarrow \quad 1s^2\ sp_3^1\ sp_3^1\ sp_3^1\ sp_3^1$$

These new orbitals are arranged in a tetrahedron shape (Figure 2.6). After the hybridization, all four orbitals have the same energy, lower than p but higher than s orbitals.

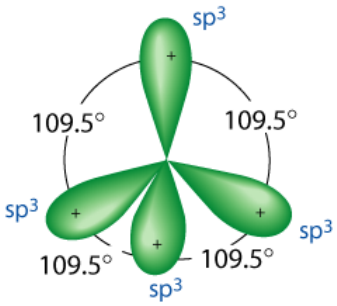

Figure 2.6: sp^3 hybridization tetrahedron shape [18].

In this configuration, all four valence electrons of carbon are occupied to form bonds, they are localized in between atomic nuclei. Consequently, there are no electrons left to conduct electrons. This is why compounds with sp^3 carbon are dielectrics, they have energy gaps: four electrons form valence band and conductance band is empty.

- sp^2 **Hybridization**

  Graphene has a honeycomb 2D shape, so it means that each carbon atom has three bonds to other carbon atoms. In this case, three atomic orbitals are mixed to form three new hybridized molecular orbitals. These new orbitals are called sp^2 hybridized orbitals, since the s and two of the three p orbitals are combined.

$$1s^2\ 2s^2\ 2p^2 \quad \longrightarrow \quad 1s^2\ sp_2^1\ sp_2^1\ sp_2^1\ 2p_z^1$$

  Because one of the p orbitals has not changed, its energy is higher than the sp^2 orbitals. Since 3 electrons form bonds (sp^2 orbitals), the one (p_z orbital) is left and contributes to the electric conductivity. For example, graphite is a metal with zero electron density at the Fermi level. This way, there are three identical bonds and due to the symmetry they have a planar trigonal geometry with 120 degrees between each other, while the remaining p orbital stays normal to its plane (Figure 2.7). In the case of graphene, only three bonds are made through the sp^2 orbitals, leaving the p orbital electron "quasi-free" and responsible for the electrical conductivity.

2.1.3.2 Production Techniques

Two types of graphene are tested and compared in this work: one produced by chemical vapor deposition (CVD) which results in a growth of mono or multilayer invisible (to bare eye) graphene sheet; the other is produced by a more exotic technique which is microwave plasma enabled synthesis of free standing graphene. Both of these techniques follow a "bottom-up" approach, in which carbon nanostructures are grown from hydrocarbon precursors.

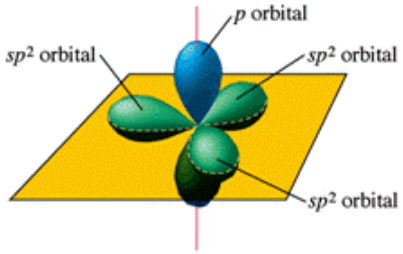

Figure 2.7: Trigonal planar geometry of sp^2 hybridization [19].

1. **Chemical Vapor Deposition (CVD)**

   CVD is one of the standard techniques for graphene production. The apparatus consists of a tubular furnace where high temperatures are achieved (900-1000 °C). Firstly an inert Ar/H_2 gas is introduced through the furnace for impurities removal that might prevent the graphene growing. Then, the hydrocarbon gas (usually methane, CH_4) is introduced (carbon precursor). At the high temperatures achieved, the hydrocarbon gas decomposes into carbon and hydrogen. The formed carbon is deposited on a copper catalyst and forms a honeycomb structure of graphene. The metal surface acts as a catalyst, so, as soon as it is covered, the catalytic effect stops. Hence the technique is more convenient to grow a single layer of graphene. These catalytic properties are only common to certain metals, which is why copper is used as a catalyst [20].

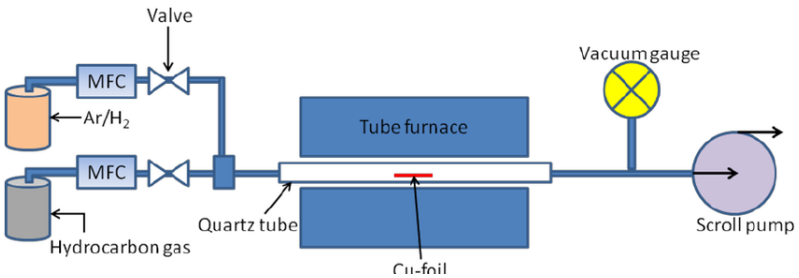

Figure 2.8: Scheme of standard CVD grown graphene [20].

2. **Microwave atmospheric plasma based synthesis**

   In comparison with CVD, plasma assisted techniques have their own advantages in carbon nanostructures' synthesis. Plasma systems possess thermal and chemical reactor functions. Using plasma to assist the growing of graphene, a catalyst is not needed, opposing the case of CVD. Plasmas have the unique ability to create favorable conditions for nucleation and growth processes [21].

   A hydrocarbon gas (ethanol vapour, C_2H_5OH) is injected into the chamber together with Ar used as a carrier gas, where a plasma environment is created. Due to the intense heating of the plasma by microwaves, collisions and extreme chemistry,

carbon atoms and molecules are created. These carbon atoms and molecules migrate to the colder plasma regions, resulting in the nucleation of solid carbon nuclei. "The main stream of carbon nuclei is gradually withdrawn from the hot plasma region into the outlet plasma stream, where flowing carbon nanostructures assemble and grow" [21]. By adjusting the microwave plasma environment, it is possible to achieve the synthesis of free-standing graphene platelets (stacks of graphene with 10 to 20 layers) [21]. IR heaters and UV irradiation are used to tune the thermodynamical conditions in the nucleation zone.

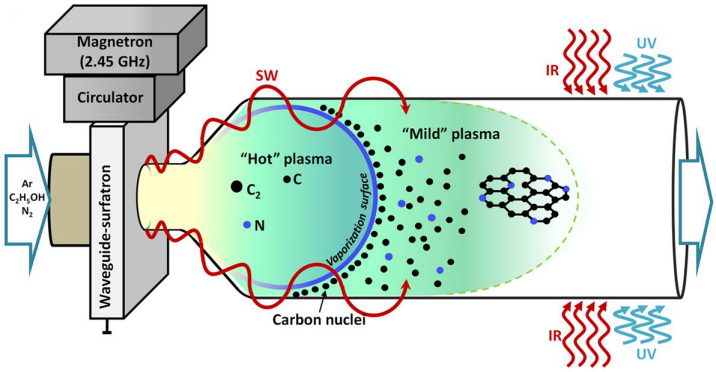

Figure 2.9: Process scheme of microwave atmospheric plasma based production of free standing graphene [22].

2.2 Experimental Techniques

This section is divided in four subsections describing the following techniques: Electrophoretic Deposition - EPD, X-ray Photoelectron Spectroscopy - XPS, SEY measurement and Scanning Electron Microscopy - SEM. EPD is used to make the graphene coatings, XPS for characterization of the surface, SEY apparatus for SEY measurement and finally SEM for the surface morphology analysis.

2.2.1 Electrophoretic Deposition - EPD

Electrophoretic Deposition consists of a dispersed powder material in a certain solvent (electrolyte) and with an applied electric field, the powder particles are able to move into a desired arrangement on an electrode surface (Figure 2.10). The electrolyte charges the surface of the dispersed particles enabling these to move according to the applied electric field. The charging process occurs via the formation of an electrical double layer (Figure 2.11). The first layer consists of ions adsorbed onto the surface due to chemical interactions. The second layer is composed of ions of the opposite charge which electrically screen the first layer by Coulomb forces. This second layer of ions is not related to the surface but to the fluid where particles are dispersed. This phenomena results in a potential difference

between the particles and the fluid (zeta potential).

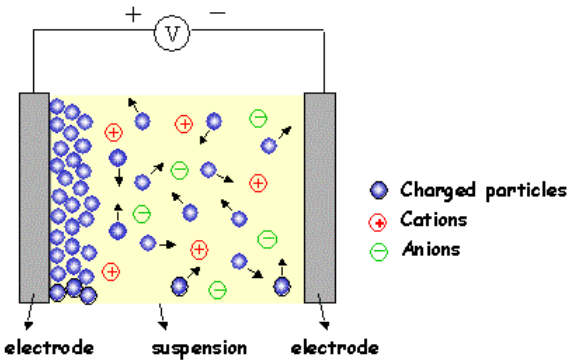

Figure 2.10: Schematic of EPD phenomena [23].

Zeta potential is the electric potential in the interface of the double layer with the fluid (Figure 2.11). It is a key factor since it plays a role in the stability of the suspension, the direction and migration velocity of particles and the density of the deposit [24]. The stability of the suspension depends on the interaction between particles, which are driven by Coulomb and Van der Waals forces. These forces define the interaction between the particles - whether if the suspension will be stable or not, and whether it will be able to deposit. The particle charge also affects the density of the deposit. If the charge is too low, particles tend to agglomerate, while if the charge is too high, particles will repulse each other leading to a non-efficient deposition. Therefore, it is important to control the zeta potential in order to achieve an efficient EPD.

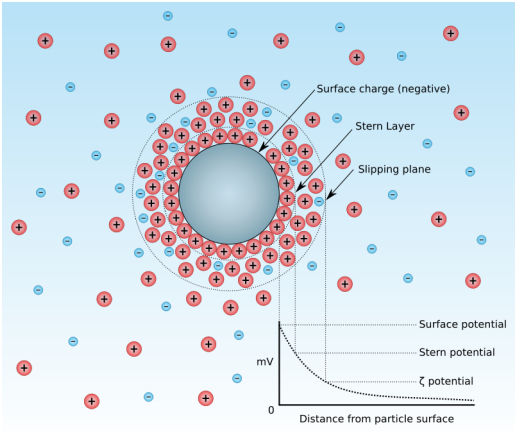

Figure 2.11: Diagram of double layer and zeta potential of a particle in an ionic fluid [25].

There are four main characteristics that define EPD:

1. **Particle dispersion**

   The first step in EPD is a stable particle suspension where the chosen particles are homogeneously dispersed and able to freely move in the electrolyte suspension. It

is important that the particle dispersion stays stable from the end of the dispersing process (sonication) to the end of the deposition. The dispersion of particles depends on Van der Waals forces, on the Debye length and the amount of charge in the first layer.

2. **Particle charging**

   The particles gain a surface charge due to the electrolyte composition where adsorption/dissolution equilibrium for anions and cations need to be different. This results in selective dissolution and adsorption of ions from the particle and the solvent, respectively. Both require a solvent able to support ionic charge (electrolyte). There are solvents that behave like dielectric which do not support dissolved ions, however, in EPD, solvents need to support dissolved ions since particles have to be electrochemically charged [26]. This factor directly affects the previous one.

3. **Electrochemical migration**

   An electric field is essential for particles in a suspension can electrochemically migrate. When a voltage is applied to the dispersion, the charged particles migrate to the opposite charged electrode, where an electrostatic boundary layer is formed. This created layer will shield the electrode's charge. similarly to a plasma, resulting in a null electric field in the bulk of the suspension [26]. This way, the electric field is confined to the boundaries of the electrode (Figure 2.12).

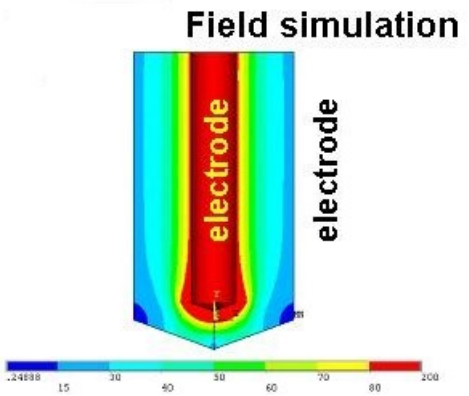

Figure 2.12: Simulation of the electric field around the electrode [23].

4. **Deposition of particles** Due to electrochemical changes occurring at the electrode, there are different phenomena that can change the balance of the dispersed particles, leading to their repulsion between each other in the suspension and their deposition at the electrode.

After studies performed in [27], it was discovered that if the suspension is too conductive, particles move very slowly, and if it is not conductive enough, particles become electronically charged and the suspension looses stability. This is the main reason why if

there is too much charge, deposition does not occur, because particles will repel each other. This results in short Debye length of the electrodes and lack of field in the suspension.

It was also discovered that there is a narrow margin of conductivity (which is different for every system) suitable for EPD. For this reason, the conductivity of the suspension needs to be carefully controlled in order to be able to use the technique. So, according to the theory, particles move and are deposited together with the ions, which stay attached to the particles.

There is one other type of electrochemical process that can be similar and easily confused with EPD, but is fundamentally different from it. This other technique is called electrodeposition (electroplating). This technique produce coatings by diffusion and migration of ions or molecules from one electrode to the other, where they are electrochemically converted into an insoluble form [26]. Typically there are dissolved metal cations, which are produced at the anode, that flow to the cathode resulting in their reduction, and consequently, in the formation of a thin uniform metal coating.

Table 2.1 resumes the main differences between EPD and electroplating.

Table 2.1: Main differences between EPD and Electroplating [26].

Deposition Technique	**Electrophoresis**	**Electroplating**
Moving Species	Solid Particles	Ions
Charge Transfer	None	Ion Reduction
Required Conductance of Liquid Medium	Low	High

Sometimes there is a type of corrosion where small cavities (pits) are created on the surface of a metal and can go all the way through without losing any thickness. They are extremely localized and their main source is the location of the oxides on the surface. If the surface is anodic, the areas where there is excess of oxygen become cathodic leading to a localized corrosion creating pits. This type of corrosion is called pitting.

2.2.1.1 Factors influencing EPD

Electrophoretic deposition deals with suspended charged particles under the influence of an electric field. There are two main groups of factors that may influence EPD: the parameters related to the suspension and the parameters related to the process [24].

In suspension properties, characteristics of the liquid such as of the suspended particles, must be considered.

- **Particle size**

  According to [28], particle size in range of 1-20 μm for ceramics and clay particles, lead to a good deposition. This does not mean that it is not possible to deposit particles larger than this. The biggest problem for larger particles is their settlement

due to gravity. This usually results in a non-uniform coating, where the bottom part of the electrode is thicker than the upper (for vertical electrodes). For this reason, particles must remain well dispersed in order to assure good mobility and uniform coatings.

- **Suspension's stability**

  The stability of the suspension is important for dispersed particles to move when an electric field is applied. Particles which are 1 μm wide, or less, tend to remain dispersed, while particles above that size require continuous hydrodynamic motion. The stability is defined by the settling rate and tendency to avoid agglomeration, where a stable suspension shows no tendency to flocculate and settles slowly [24]. In that sense, stability is directly related to particle charge or zeta potential i.e. about the potential distribution between particles (interplay between Van der Waals and Coulomb forces).

There is one main parameter related to the process in this work, that may influence the EPD: the applied potential to the electrodes. Usually, an increase of applied voltage leads to higher deposition rates, which increases the amount of deposit, but its quality may suffer [24]. According to [29], moderate applied electric fields result in more uniform deposits, while the opposite occurs for increasing applied potentials. The increasing of the applied voltage may cause turbulence in the suspension leading to undesirable flows in the fluid, which disturb the deposition process. Due to the higher depositions rates, particles might move too fast and they would have not enough time to properly fix to the electrode. In conclusion, the applied potential directly influences particle flux, consequently affecting the deposition rate and the structure of the deposit [24].

2.2.1.2 Home-made EPD system

The home-made apparatus built for electrophoresis is composed of 4 pieces (Figure 2.13):

- **Electrodes**: two metal plates responsible for creating the electric field. They are both 20x10 mm and they are 15 mm away from each other. Flat plates were chosen so they could be measured properly in XPS, SEM and SEY. The counter electrode (uncoated) is gold, one of the most inert metals for electrolysis, despite stainless steel was also used, and the coated electrodes were stainless steel and copper.

- **Conductive rods**: these are two identical copper wires, 2 mm thick, where the electrodes are attached on one end. The opposite ends are connected to the power source

- **Rubber support**: this piece is responsible for holding everything together. Additionally, it defines the geometry of the system. It has two tight holes, where the copper rods are fixed and a third and bigger hole for gas exhaustion.

- **Glass cup**: the glass cup is needed to sustain the electrolyte and it is where the rubber support is attached.

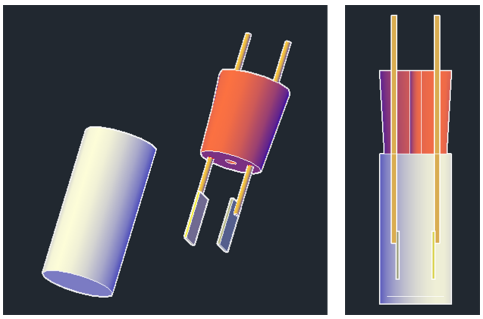

Figure 2.13: Home-made apparatus for EPD.

2.2.2 SEY apparatus

2.2.2.1 Operation Principles

The apparatus measures the secondary electron yield by measuring independently the emitted and incident current. In this setup, sample is mounted on a sample holder, which is placed inside of a Faraday cup. Initially, the sample holder is negatively biased (-V), to repel secondary electrons from the sample and suppress the arrival of the second generation of secondary electrons produced on the walls of the Faraday cup. That way, the secondary electron current generated by the sample is measured by the Faraday cup (I_{FC}). This measurement has the contribution of secondary electrons (I_s) and backscattered electrons (I_b) (Figure 3.3: left).

$$I_{FC} = I_s + I_b \tag{2.12}$$

Secondly, a shortcut is made between the sample holder and the Faraday cup and the current is again measured. Since everything is now connected (sample holder becomes integral part of the Faraday cup), the primary electron current (I_p) is measured (Figure 3.3: right).

With these two measured currents, SEY is the quotient between the first and the second magnitude.

$$\delta = \frac{I_{FC}}{I_p} = \frac{I_s + I_b}{I_p} \tag{2.13}$$

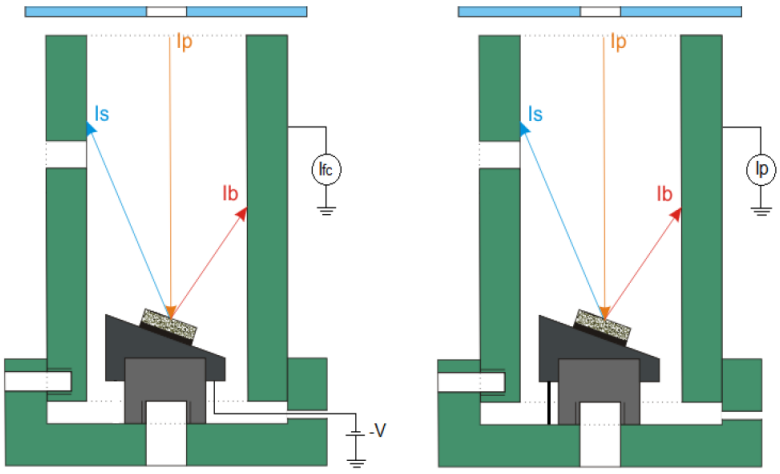

Figure 2.14: Measuring method of primary and secondary currents [4].

2.2.2.2 Instrumentation

The home-made apparatus for SEY measurement is composed of few main elements (Figure 2.15) that will be identified ahead:

- **External support** (Figure 2.15: yellow): this component is responsible for holding everything together. It is split into two parts so it can be possible to exchange samples. Its closed structure provides electrical shielding of the whole system and therefore reduces the noise.

- **Insulating cylinder** (Figure 2.15: light grey): this cylinder is made of alumina which provides an electric isolation between the Faraday cup and the external support. This isolation is very important so the measurement of both currents can be correctly made.

- **Sample holder** (Figure 2.15: dark grey): this is the piece where the sample mounted. It is supported by a small alumina cylinder so it can also be isolated from the Faraday cup to prevent a shortcut between them. As already explained, the sample holder can be shortcut to the Faraday cup or biased negatively to help the secondary electrons being ejected from the sample into the Faraday cup and to suppress arrival of the secondary electrons from the Faraday cup to reach the sample (and therefore decrease the measured current of secondary electrons from the sample).

- **Electron gun** (Figure 2.15: dark blue): this part is a typical electron gun with an hairpin geometry filament followed by electron optics for the beam focusing.

- **Suppressor electrode** (Figure 2.15: light blue): this electrode is negatively biased so it can suppress all the electrons that try to escape from the Faraday cup.

- **Faraday Cup** (Figure 2.15: green): the cup is also split into two parts with the same purpose as the external support. The Faraday cup is the detection system of the apparatus since it is the electron collector. The current generated is measured by an electrometer connected to the cup.

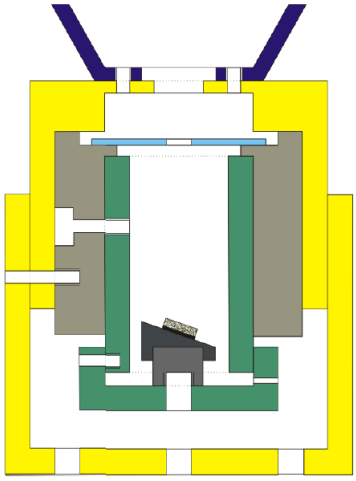

Figure 2.15: Instrumentation layout of the homemade apparatus for SEY measurement [4].

2.2.2.3 Measuring Errors

The secondary current I_s in SEY is the current generated in the Faraday cup by the secondary electrons emitted from the sample surface (when the sample is biased) or the primary electron sample (when the sample and the Faraday cup are in shortcut). In an ideal case, when the electron beam only hits the sample, the main measurement error is related to the electron beam stability and the measurement uncertainty of the two currents. However, frequent work with the equipment revealed another potential systematic error, which takes place when part of the primary electron beam misses the sample and hits the bottom of the Faraday cup (Figure 2.16). The amount of this error can be analytically estimated.

Primary current I_p is defined as the current generated by the electrons that hit the sample, I_p^S, plus the ones hitting the Faraday cup, I_p^F:

$$I_p = I_p^S + I_p^F \tag{2.14}$$

Being $I_p^S = (1-k)I_p$ and $I_p^F = kI_p$, assuming k is the fraction of primary electron current that misses the sample. Using equation (2.14):

$$I_p = (1-k)I_p + kI_p \tag{2.15}$$

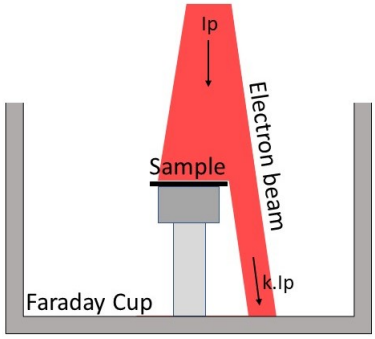

Figure 2.16: Illustration of SEY measuring errors.

In that sense, the measured secondary current is the sum of two contributions: the primary electrons that hit directly the Faraday cup (miss the sample), I_p^F, and the secondary electrons generated on the sample.

$$I_s = I_p^F + I_p^S \delta \tag{2.16}$$

with $\delta = \frac{I_S}{I_p^S}$ being the real SEY of the material. So, combining equations (2.15) and (2.16),

$$I_s = kI_p + (1-k)I_p\delta \tag{2.17}$$

Considering δ_{exp} what is really measured:

$$\delta_{exp} = \frac{I_s}{I_p} = \frac{kI_p + (1-k)I_p\delta}{I_p} = k + (1-k)\delta \tag{2.18}$$

Taking equation (2.18) into consideration, some conclusions can be drawn:

- If δ is below 1, the measured magnitude δ_{exp} is greater than the true value;
- If δ is above 1, the exact opposite occurs, δ_{exp} is lower than the expected value;
- If k is 1, which means the beam is completely missing the sample, δ_{exp} is going to be exactly 1;
- Finally, if the entire beam hits the sample ($k = 0$), then $\delta_{exp} = \delta$.

Clearly the value of k depends on the size of the primary beam spot. Our experience shows that eventual problems with this kind of error appears when the primary beam current exceeds 10 nA. Consequently, we were always tending to work with low intensity and stable beams. Another advantage of reducing the primary beam intensity is to suppress eventual sample modification (via electron stimulated desorption and other effects).

2.2.3 X-Ray Photoelectron Spectroscopy

2.2.3.1 Operation Principles

XPS is based on the photoelectric effect but the irradiation of the sample can lead to the occurrence of two different phenomena: emission of photoelectrons and Auger electrons (Figure 2.17). The X-rays interact with the atoms of the surface, exciting them, and if they have enough energy, they are ejected from the inner shells of the atom. These photoelectrons have a kinetic energy (E_k) equal to the difference between the X-ray energy ($h\nu$), the binding energy of the emitted electrons (E_b) and the work function of the energy analyzer:

$$E_k(e^-) = h\nu - E_b - WF_{anal} \tag{2.19}$$

After the ionization, the electron cloud can rearrange itself by radiative or non-radiative processes. In the second case, the ion has some potential energy which is spent to the emission of electrons. The driving force for the emission is Coulomb repulsion between the two electrons in the atom. This emitted electron is called Auger electron.

$$E_{IJK}(e_A^-) = E_{bI} - E_{bJ} - E_{bK} - WF_{anal} \tag{2.20}$$

where E_{bI}, E_{bJ} and E_{bK} are respectively the binding energies of the core level (from where the inner electron was ejected), first outer shell, and second outer shell (energy level where Auger electron came from).

The XPS spectra will be mainly composed of photoelectronic peaks but will also have Auger electron contributions resulting in two different kinds of peaks in a final spectrum.

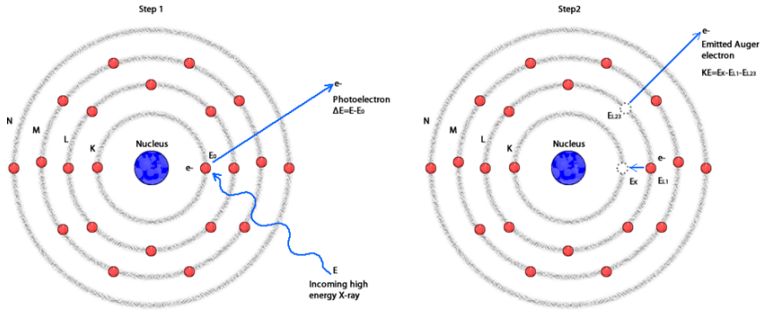

Figure 2.17: Schematic of photoemission process and Auger effect.

On the course of the electrons from the interior of the material to the surface, the main mechanism of the energy loss is the excitation of valence electrons. XPS and AES peaks correspond only to the electrons that did not lose energy. Emitted secondary electrons created inside the material contribute to a specific background shape of the spectrum.

The binding energy of the emitted electrons depends on their main quantum number and total angular momentum j:

$$j = l + s \tag{2.21}$$

in which E_b decreases with j. Therefore, for each single electron orbital there are two lines corresponding to the two values of the angular momentum. The exceptions are s orbitals ($l = 0$) when the total angular momentum can be only $j = 1/2$. There are $2j + 1$ degenerate states per each j, which provides the correlation between the number of states and the intensity ratio between the two peaks attributed to a single electron orbital. For example, if an electron ejected from a p level reaches the detector, it will result in two spectral lines ($j = 3/2$ and $j = 1/2$), so that the $3/2$ peak has twice the intensity of the $1/2$ peak (2:1). The intensity ratios between the lines having the same main and orbital quantum number are summarized in Table 2.2.

Table 2.2: Correlation between the degenerate states and respective intensity ratios.

Energy level	**l**	**j**		**Intensity ratio**
s	0	1/2		-
p	1	3/2	1/2	2:1
d	2	5/2	3/2	3:2
f	3	7/2	5/2	4:3

2.2.3.2 Instrumentation

The X-ray photoelectron spectrometer has 4 main components (Figure 2.16):

1. **X-Ray source**: the apparatus that will be used has a double non-monochromatic anode source of Al/Mg K_α. The advantage of these kind of sources, besides the possibility to change between anodes, is that it facilitates the charge accumulation effect on the non-conductive samples, but its resolution is worse than of a monochromatic source. The two anodes have similar photon energies to observe the differences between Auger and photoelectric peaks. In the kinetic energy scale, photoelectric peaks shift for different photon energies and Auger peaks do not. In the binding energy scale, they have the opposite behavior.

2. **Hemispherical energy analyzer**: this type of analyzer only allows electrons of a certain energy to reach the detector. This pass energy inside the analyzer is defined by the voltage applied between the two hemispheres. The energy is determined by the difference between the potentials of the sample surface and the entrance slit into the analyzer. This method, where the pass energy of the analyzer is kept constant, is called FAT (Fixed Analyzer Transmission) and it allows to keep the resolution and the transmission of the analyzer constant with respect to the electron kinetic energy.

3. **Electron detector**: the signal generated by the electrons that reach the detector is converted in an electric signal. To do so, it is used a Channel Electron Multiplier (CEM) or Channeltron.

4. **Vacuum System**: ultra-high vacuum is necessary to keep the surface of the sample clean and for an efficient functioning of the X-ray source. Surface cleanness is essential due to the very high surface sensitivity of the technique: the information depth of XPS is typically 5-10 nm. Another reason to keep the system under vacuum, although less demanding than the other two, is to increase the mean free path of the electrons on their way from the sample to the detector.

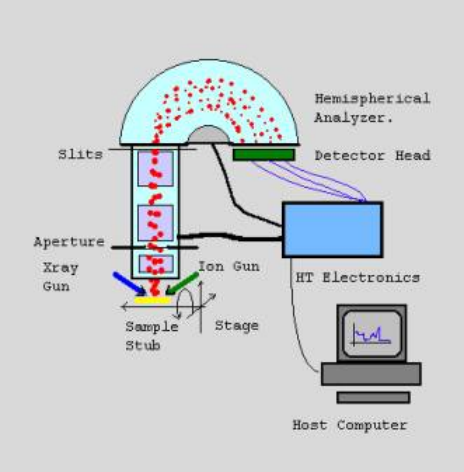

Figure 2.18: Instrumentation layout of a typical XPS instrument [30].

2.2.3.3 Chemical Information

Composition Determination

Elemental composition analysis can be obtained from the intensities of characteristic peaks of each element at the surface. The peak intensity of an element, S_i is proportional to: photon flux, I ($m^{-2}s^{-1}$), acquisition time per energy channel, Δt (s), analyzed area, A (m^2), photoemission cross-section, σ_ν (m^2), effective attenuation length, λ_i (m), detection efficiency, D, transmission of the spectrometer, T, and concentration of the element, n_i (m^{-3}) [31]. Assuming uniform depth distribution of the concentration ($n_i(z) = N_i$), the total XPS signal can be calculated from,

$$S_i = I \cdot \Delta t \cdot A \cdot D \cdot T \cdot \sigma_i \cdot \lambda_i \cdot N_i \tag{2.22}$$

In many cases, composition analysis is based on the upper formula, although sometimes the assumption of uniform depth distribution is not correct. This way, relative

sensitivity factors (SF) may be determined by performing measurements on a reference sample.

$$SF_i = \frac{S_i^{ref}}{I \cdot \Delta t \cdot N_i^{ref}} = A \cdot D \cdot T \cdot \sigma_i \cdot \lambda_i, \tag{2.23}$$

where N_i^{ref} is the bulk concentration of the reference sample.

It is more convenient to define sensitivity factors relative to one element, for that purpose, fluorine is frequently used ($RSF_F = 1.0$). Consequently, relative sensitivity factors of any element is defined as

$$RSF = \frac{SF_i}{SF_F} = \frac{S_i^{ref}/N_i^{ref}}{S_F^{ref}/N_F^{ref}} \tag{2.24}$$

Finally, relative concentration of an element 'i' is determined as

$$c_i = \frac{S_i/RSF_i}{\sum(S_j/RSF_j)} \tag{2.25}$$

where index 'i' is related to the element and 'j' to all elements identified in the sample. This last formula is used for composition analysis in XPS in the vast majority of cases.

Chemical Shifts

The chemical shift of photoelectron peaks is related to the difference in position of a photoelectron peak for atoms of the same element in different chemical environments. For example, considering a lithium atom in a clean metal (Li) and in its oxide (Li_2O): due to the electronegativity of the oxygen (O), the valence electrons of Li will move towards the O atoms. The remain electron in the Li atoms will have higher binding energies due to the lack of electrons which partially screens the attractive force of the nucleus. This effect leads to higher binding energies in the clean metal compared to the Li_2O, which means there is a shift of the lithium peak in that direction [32].

Modified Auger electron parameter

Besides the photoelectron lines, Auger lines sometimes also have chemical shift. As the matter of fact, the chemical information is extracted from the relative position of the most intense photoelectron and Auger line of a specific element. In practice, an equivalent magnitude, denoted modified Auger parameter is defined as the sum of the photoelectron line binding energy and the Auger line kinetic energy. The advantage of using this magnitude is that it is invariant to the applied photon energy. So, when using this approach, the modified Auger parameter is much less affected by the sample charging phenomena, which take place in the case of non-conductive samples, as compared to the exact position of a photoelectron line [33].

Shake up Satellites

Usually it is assumed that there is no rearrangement of the electron cloud after an electron emission. In this case, the electron binding energy is the same as the energy of the level where it came from. In some cases, there is a probability that some of the photon energy is spent exciting an electron from upper levels. In this situation, the energy of the photoelectron is reduced, which results in a higher binding energy and the respective peak is preceded by a shake-up satellite. At first sight, this energy loss complicates the spectrum analysis but the position and the intensity of the shake-up satellites strongly depend on the chemical bonds, so these can be used as fingerprints of some chemical compounds [34].

Multiplet Splitting

Multiplet splitting occurs when an atom has unpaired electrons. When an inner shell electron vacancy is created by photoionization, an unpaired outer shell electron can be coupling with the unpaired core electron. These phenomena create different final states which contribute to a multipeak envelope in the final spectrum [31]. Cr $2p_{3/2}$ line for a Cr_2O_3 sample is a good example of multiplet structures (Figure 2.19).

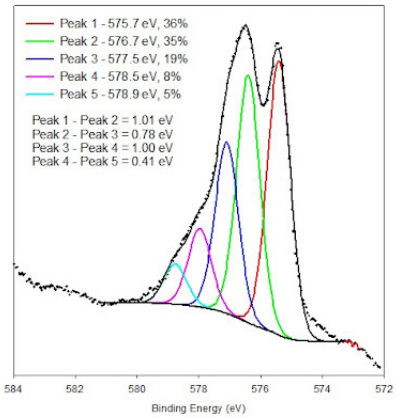

Figure 2.19: Multiplet structure associated with the Cr $2p_{3/2}$ peak for a vacuum fractured Cr_2O_3 specimen [35].

Profile Lines

In XPS analysis, a wide variety of line profiles can be used to fit XPS spectra, and simple Gaussian or Lorentzian functions are very rarely used. In some cases, asymmetric profiles are theoretically expected, but due to instrumental and physical effects, real XPS data show some deviations from the theory [36]. Some of these effects can be: the response function of the analyser, profile of the X-ray line-shape (dependent of whether it is monochromatic or non-monochromatic), differential surface charging of the sample, among others.

In this work, 3 different line shapes are used for the fitting of the XPS spectra:

- Gaussian-Lorentzian(product) - GL(p)

  This profile is a pseudo-Voigt profile in the form of a product of Gaussian and Lorentzian. Voigt profile is the convolution of Gaussian and Lorentzian, but this integral does not have analytical solution. That is the reason why Voigt profile has to be simulated as a product of G and L, (GL profiles) or as a sum of G and L (SGL profiles). So these are approximations of the Voigt profile which is theoretically expected in many cases. GL(p) is a Gaussian/Lorentzian product where the mixing is determined by p (percentage of Lorentzian contribution). So GL(100) is a pure Lorentzian while GL(0) is pure Gaussian [36].

$$GL(x, F, E, m) = \frac{\exp(-4ln(2)(1-m)\frac{(x-E)^2}{F^2})}{1+4m\frac{(x-E)^2}{F^2}} \tag{2.26}$$

  Throughout this work, this line shape is used to fit almost every peak and its contributions in XPS spectra.

- Doniach-Šunjić - DS(α,n)

  DS(α,n) is a basic Doniach-Šunjić profile convoluted with a Gaussian. α is an asymmetry parameter and n is the the convolution width, related to the Gaussian's width. This profile is theoretically predicted for the photoelectron lines emitted from metallic samples. Convolution with Gaussian is used to include the contribution of the finite resolution of the energy spectrometer. This line shape is typically used for fitting doublets, and it will be used further to model the Au 4f doublet profile.

$$DS(x, \alpha, F, E) = \frac{cos[\frac{\pi\alpha}{2} + (1-\alpha)tan^{-1}(\frac{x-E}{F})]}{(F^2+(x-E)^2)^{\frac{1-\alpha}{2}}} \tag{2.27}$$

- Hybrid Doniach-Šunjić/Gaussian-Lorentzian(product) - H(a,n)GL(p)

  H(a,n)GL(p) is a hybrid form of DS/GL convolution an it is similar to DS(a,n)GL(p), only differing the FWHM and area parameters that are determined by the curve shape. The asymmetry parameter, a, is defined as

$$a = 1 - \frac{fwhm_{left}}{fwhm_{right}}$$

  This hybrid profile is use to fit the C1s graphitic line. The parameters were determined by us from fitting C 1s line of Highly Oriented Pyrolytic Graphite (HOPG), using it as a reference for C 1s of sp^2 carbon.

2.2.4 Scanning Electron Microscopy

2.2.4.1 Operation Principle

Scanning electron microscopy (SEM) is a powerful technique for the observation of small objects, including the characterization of surface morphology. SEM's operation principle

consists in using an electron beam, guided by a deflection system that allows a scanning of the sample's surface. The electrons of the beam can be produced by a heated filament that works typically from 1 to 50 kV, or by field emission where emission of electrons is induced by an electrostatic field. The created electrons are accelerated and focused on the sample.

Once the electrons interact with the material of the sample, three types of phenomena are used to characterize it (Figure 2.20):

1. When primary electrons hit a bound electron (Figure 2.20: left), they can ionize the atom by ejecting an electron. As the matter of fact, the closer is the binding energy to the primary ion energy the higher is the ionization probability. But then the ejected electron, with much less energy, will go away. Finally, after several generations, many slower electrons which loose their energy through different processes, are responsible for generating secondary electrons.

2. Backscattered electrons are electrons emitted from the surface with energy above 50 eV. These electrons are primary electrons that lose, or not, some of their energy before being backscattered (Figure 2.20: middle).

3. High energy primary electrons can excite inner shells electrons, creating a hole. One of the electrons from the orbitals immediately above descends and occupies the vacancy. This transition results in the emission of electromagnetic radiation (characteristic X-rays) (Figure 2.20: right).

All of these effects have their respective detection systems which contribute in their own way for the imaging process.

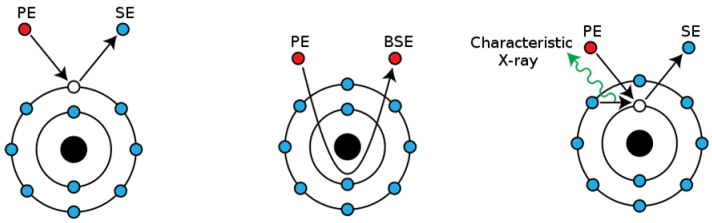

Figure 2.20: Mechanisms of secondary electrons emission, backscattered electrons, and characteristic X-rays from SEM's samples [37].

2.2.4.2 Instrumentation

A typical SEM instrument has a few main components that are fundamental for the equipment (Figure 2.21):

- **Electron gun**: the electron gun is composed of an electron emitter, where the electrons are created by thermionic effect or field emission, and a set of electrodes which are responsible for their extraction and acceleration to create the beam.

- **Focusing system**: this is a set of electrodes responsible for the focusing of the electron beam.
- **Scanning coils**: these are deflection coils which are placed at the end of the focusing system and its function is to deflect the beam in the xy plane so it can scan and raster an area of the sample surface. Magnetic fields typically produce much stronger force than electric fields. When dealing with very fast electrons, a huge force to deflect them is needed. It is much easier to do that by a small applied current in a coil than by a great applied voltage to deflection plates.
- **Detection system**: usually there are two types of detection systems, secondary electron detector which is indispensable, and a backscattered electron detector. The secondary electron detector is used to distinguish between areas with different depths, where darker areas are deeper than the brighter ones. This is explained by low secondary electron emission from deeper zones (dark areas) where secondary electrons are recaptured, while superficial areas have higher secondary electron emission (brighter zones). The second detection system is used to detect contrast between areas with different chemical compositions. Since heavy elements backscatter electrons more strongly than light elements, resulting in brighter areas on the image. It can also have an x-ray detector so it can perform EDS (Energy Dispersive X-ray Spectroscopy) for chemical analysis.
- **Vacuum system**: electronic microscopes should operate at least at 10^{-6} mbar. This guarantees a longer free mean path, for the secondary electrons to travel from the sample to the detector, eliminate discharges between the anode and the cathode and extends the filament "life". Ion pumps secure the best pressure in the region close to the electron source, where the acceleration takes place. The necessity of vacuum makes it impossible to scan wet samples.

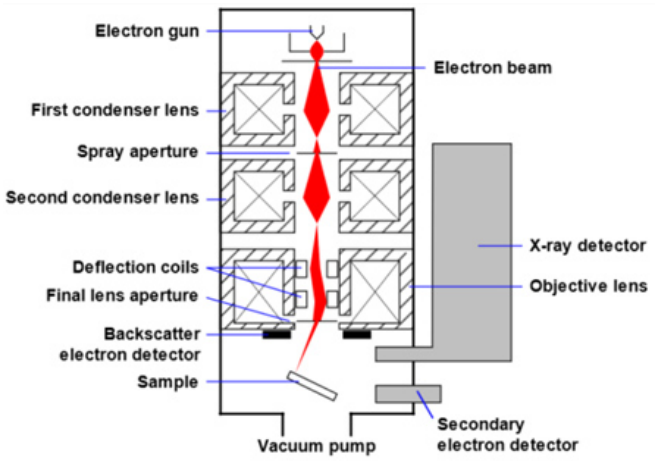

Figure 2.21: General schematic of a SEM's instrumentation [38].

CHAPTER 3

EXPERIMENTAL PROCEDURES

There are two important experimental procedures that are worth to be described: the production of the coatings by EPD and the SEY measurement.

3.1 EPD procedure

The EPD technique was chosen because it was proven that graphene coatings by EPD could reduce the SEY of a surface material [3]. Since it is an extremely simple and cheap technique and can be applied to both small and large scales, it was a very promising option. For that reason an EPD cell was built (Section 2.2.1.2). The various choices and parameters used in this technique were a combination of different references in the literature.

Firstly, the choice of electrodes was made according to the interest of this work. It was used copper (Cu) and stainless steel (SS) plates, 0.4 and 1 mm thick, respectively, as the coated electrode and a gold (Au) foil, 0.1 mm thick, as the counter electrode. Gold or gold coated electrodes are commonly used in electrophoretic deposition because it is one of the few materials that are most inert to electrochemical processes, similar to platinum [39].

Secondly, the electrolyte was chosen based on [3] and [39]. The first reference studies the influence of graphene coatings produced by EPD in SEY of a certain material. It is used a mixture of water with hydrochloric acid (HCl) as electrolyte for dispersing graphene. The second reference studies graphene dispersions in low boiling solvents aiming to optimize the dispersion procedures for spray coating techniques. According to this study, all 6 different solvents (Acetone, Chloroform, IPA-Isopropanol, Cyclohexanone-CHO, N-methyl-pyrrolidone-NMP and dimethylformamide-DMF) used, despite their differences in dispersive and concentration parameters, worked regarding dispersing graphene. Due to the many failed trials of dispersing free standing graphene on water (different sonication

times and equipments), trying to reproduce the procedure in [3], an alternative had to be taken. In that sense, an experiment of trying to combine both studies was made. Instead of water as a dispersive agent, isopropanol was used. It was possible to successfully disperse free standing in IPA in about 30 seconds, leading to a completely homogenuous black dispersion. The only problem with this choice of solvent is the fact that the suspension only stays stable for approximately 15 minutes, having the need to be sonicated every 15 minutes.

The next step was to add the source of ions to make the electrolyte, so, 20 μL of HCl were added to the 7.5 mL of isopropanol. The amount of HCl was studied according to the current obtained in the deposition process and the amount of chlorine (Cl) contamination on the coating. For that reason, an amount between 10 and 20 μL was the minimum amount to get a minimal stable current and the maximum amount to not get significant chlorine contamination ($< 1\%$).

Finally, it had to be studied the voltage at which the process was possible. The study of the used voltage and the amount of HCl in the electrolyte were made together. Different voltages were tested regarding different amounts of HCl in the solution. In order to get current, the voltage regarding the process or the amount of HCl needed to be increased. Since the amount of HCl was chosen, because of the reasons explained above, the minimum voltage which enables to coat was found. It was concluded that 20V was the minimum voltage to get some kind of current in the "inner" circuit of EPD, resulting in 0.01 A with the 20 μL of hydrochloric acid added to IPA.

The entire process can be resumed in just a few steps as illustrated in figure 3.1.

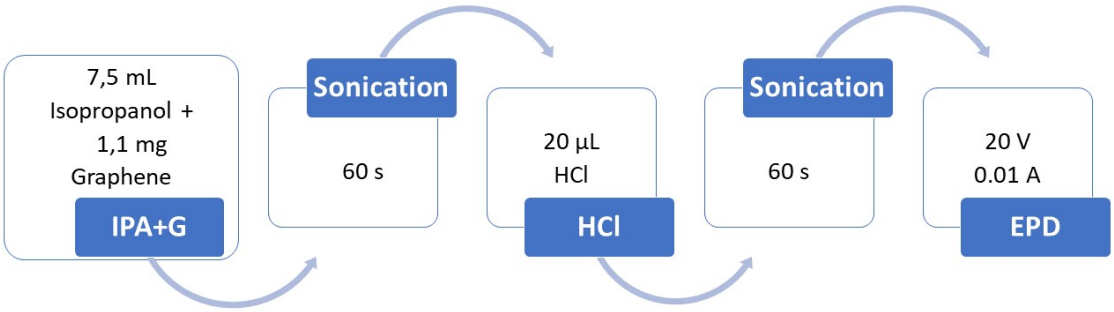

Figure 3.1: EPD procedure diagram.

Firstly, 7.5 mL of isopropanol are poured in the glass cup along with 1.1 mg of free standing graphene. The mixture is sonicated for 60 s in order to disperse homogeneously the graphene. Then, 20 μL of HCl are added followed by another 60 s of sonication. Finally, the dispersion is ready for EPD. During the EPD, depending on the deposition time, it is needed to sonicate the dispersion every 15 minutes to keep it stable, since it is not possible to perfectly stabilize it. After the deposition is complete, the sample is let to dry by air

exposure for a few minutes and it is ready to be analyzed and measured.

3.2 SEY measurement procedure

The SEY measurement procedure is much more simple than the previous one. Once the sample has completely dried from the EPD, it is immediately ready to be mounted and put under vacuum. In order to be mounted, some steps need to be taken.

The external support and the Faraday cup are divided into two parts in order to mount and dismount it. Firstly, the bottom part of the external support and the Faraday cup are detached so it is possible to mount the sample on the sample holder. The sample is held with a carbon sticker and a thin wire is attached to both sides of the sticker to ensure electrical contact between the sample and the sample holder. After the sample is mounted, everything is put back together in its proper order, the biasing contacts are checked and the chamber is closed. To create vacuum, two different pumps are used: a diaphragm pump and a turbo/drag pump to primary ($\sim 5 - 10$ mbar) and high vacuum (10^{-7} mbar), respectively. It is relatively fast to achieve high vacuum, where it is possible to go down to 10^{-6} mbar in approximately 15 minutes. After the necessary vacuum is reached and all the contacts are checked, the measurement can take place. This process is resumed in figure 3.2.

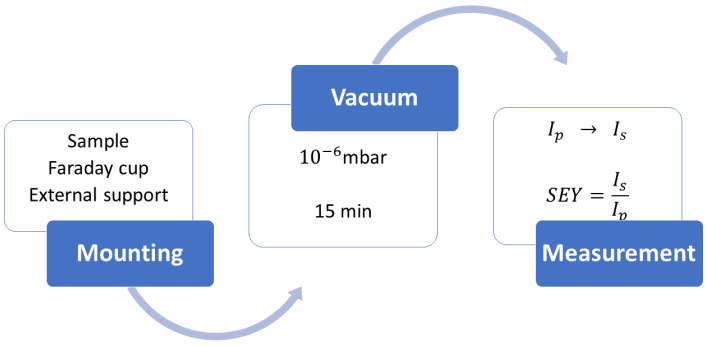

Figure 3.2: SEY measurement procedure diagram.

Two different power supplies are needed for the biasing: one polarizes the sample to -15 V and the other one the suppressor to -20 V. The sample is biased during the entire process, while the suppressor is grounded from 0 to 100 eV, low energy regime, and it is biased from 100 to 1000 eV (primary energy), high energy regime. An electrometer is connected to the Faraday cup in order to measure the low currents produced, of the order of nA (10^{-9} A). Primary and secondary current are measured independently, via a switch, as described in section 2.2.4.1. In order to go from 40 to 1000 eV (for energies below 40 eV, the current measurement is not reliable), the measurement is made in steps: in low energy regime, both currents are measured every 20 V and for high energies 50 V steps

are used. So, a total of 44 current values are taken, 22 for I_p and 22 for I_s. These values are then put into a table in any spreadsheet editor allowing an easy calculation of SEY and further drawing of its curve as a function of primary energy (Figure 3.3).

Energy eV	Ip nA	Is nA	SEY Is/Ip
40			
...			
100			
...			
1000			

(a) Example of a typical table used for SEY calculation.

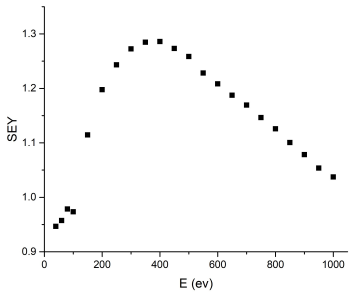

(b) Typical SEY curve.

Figure 3.3: Typical results of a SEY measurement.

CHAPTER 4

RESULTS AND DISCUSSION

This chapter summarizes all results obtained and their discussions. It is divided in eight sections, encompassing the free-standing graphene deposition results obtained with the two used substrates, two different counter electrodes, and different sets of EPD parameters. The free-standing graphene used in this work was produced using the technique presented in point 2 of section 2.1.3.2 and was acquired from IPFN-IST. The samples with the best results in terms of SEY are analyzed and discussed in detail. Besides, the consequences of EPD on the counter electrode are studied. Finally, three alternatives to graphene coatings are explored and discussed.

Since the surface characterization relies on XPS analysis, the first step of this research was to establish a reference for the C 1s line shape of the sp^2 contribution. For that purpose, freshly cleaved Highly Oriented Pyrolytic Graphite (HOPG) was used. SEY of this material was also measured in order to test the measurement equipment, since the maximum of SEY and its position, as well as the overall shape of the curve, are known from the literature. SEY of pure graphene is measured in order to see what would be the SEY limit (infinitely thick fully covered graphene coating) of the coating. At the same time, XPS of the graphene sample has been performed in order to determine the amount of defects and impurities. For that purpose, C 1s line was fitted using the line shape established on the XPS results of HOPG. Then, when deposited samples are produced, they are compared with graphene (XPS) to see if extra defects and impurities were introduced. The composition analysis of all data was performed using the standard approach i.e. assuming that the samples are uniform. Of course this is not the case, so that the results obtained should be considered as a relative measure of the amounts of different elements. All pure carbon contributions are encompassed by three main contribution: sp^2 (characteristic of graphene), sp^3 (defects) and the $\pi - \pi^*$ shake up satellite. All other contributions are related to oxygen contaminations.

HOPG XPS analysis reveals an extremely low amount of oxygen was detected ($\sim$1

%) leading a low contribution in the C 1s line. Since the C 1s cannot be fitted to two contributions, narrow asymmetric for the sp^2 bonds and a symmetric wide for the shake up satellite, a peak model previously obtained on the same system [40] was used. C 1s line presented in figure 4.2(a) was fitted to three contributions. Two of them have the same shape and width, since these features are characteristic of the sample electronic structure. The dominant line at 284.5 eV, with the relative intensity of 94.7 %, can be readily attributed to sp^2. The minor line at 286.0 eV (2.1 % of the relative intensity) is most probably related to the C-OH or C-O-C bonds [41]. Finally, the relative intensity of the shake up satellite is about 3.2 %.

A reference sample of free standing graphene obtained from IPFN-IST was created by pressing a few milligrams of graphene powder onto a lead substrate (soft metal) in order to be measured and analyzed. Concerning its morphology, with SEM it is possible to clearly see disordered sheets entangling each other. The sample contains only graphene sheets which have characteristic curled/wavy morphology, consisting of a thin wrinkled structure (Figure 4.1).

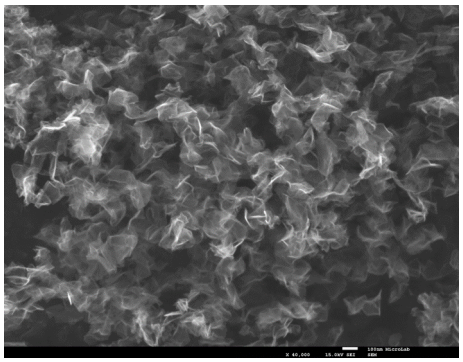

Figure 4.1: SEM image of free standing graphene sheets produced in IST [22].

The same sample is used as a reference for the XPS measurements: in an ideal case, XPS spectra of deposits should be the same as that of the free-standing graphene. The expected positions of different C 1s line contributions are as follows. The sp^2 carbon peak is supposed to be at ∼284.5 eV [42]. The sp^3 carbon and $\pi - \pi^*$ satellite peaks are constrained to a 0.8 and a 6.4 eV shift, respectively, from the sp^2 peak [42]. Oxygen contributions in C 1s are located between sp^3 and $\pi - \pi^*$ satellite and are presented in table 4.1. These fitting parameters are used for all sp^2-based systems.

Table 4.1: Peak position of O contributions in C 1s line fitting [43].

Peak	**B.E. Range (eV)**
C-OH, C-O-C	286.3 - 286.7
C=O	287.8 - 288.3
O-C=O	289.0 - 289.5

As already mentioned, the line shape is a consequence of the wider chemical environment - it is related to the electronic structure of the material through which photoelectrons

are passing. Although sp^3 features and different C-O bonds are defects, the electrons are surrounded by free electrons of graphene, which is why it is adopted the same shape and the same FWHM of all lines (except $\pi - \pi^*$ satellite).

Looking at its XPS spectra, C 1s line has contributions of sp^2 (74.5 %), 18.5 % of sp^3 defects, 4 % of $\pi - \pi^*$ satellite and 3 % of C-OH and C-O-C bonds (Figure 4.2(b)). This is coherent with the O 1s line, where 47 % is adsorbed water but the other 53 % fit well with organic oxygen. The more common organic oxygen species (alcohols, esters, ketones, ethers and organic acids) are found in a range from 532.0 - 533.7 eV while water is found at 534.4 eV [44]. This sample will be further used as a reference for future samples. Since the amount of oxygen present in the graphene sample is very low, the major difference between graphene and HOPG is the sp^3 contribution, which can be seen in figure 4.2. It is reasonable since HOPG is atomically "flat" and in the case of graphene, its production method does not assure that only sp^2 carbon is being created. Besides, dangling bonds always exist at the end of the graphene flakes, which can be saturated with sp^3 structures.

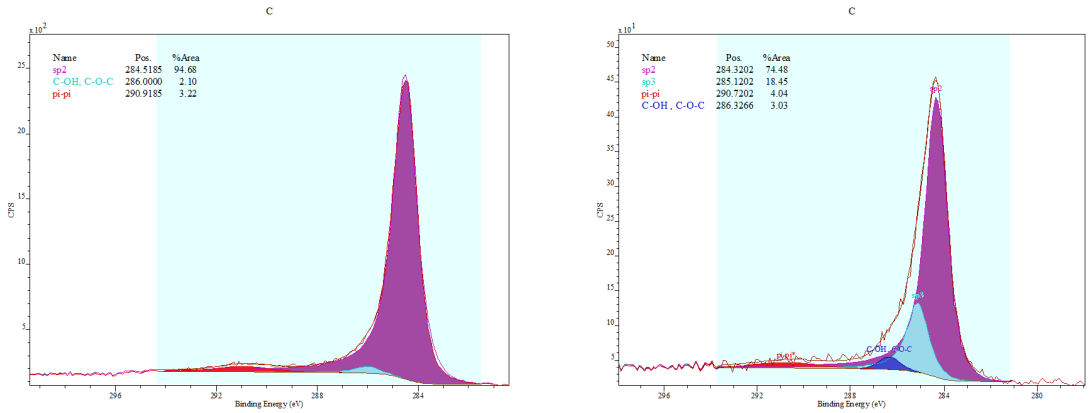

(a) HOPG (b) Graphene

Figure 4.2: Carbon 1s line of HOPG and free standing graphene.

The results of the SEY measurements from freshly cleaved HOPG and pure graphene are shown in figure 4.3. Graphene sample was prepared in the same way as for the XPS analysis. Maximum SEY of graphene is lower for about 20 % with respect to that of HOPG. Particularly interesting is in the very different shape of the SEY curve in the two cases. SEY signal obtained from HOPG has a shape typical for flat surfaces (the shape is similar to the theoretical one presented in figure 2.2), while that of graphene is characterized with slowly decaying tail after the maximum. The later is typical for rough surfaces [45].

In addition, SEY of N-doped graphene was also measured. This kind of graphene was also produced as explained in point 2 of section 2.1.3.2 but it was post treated (post-doped) with a N_2-Ar plasma (N_2:Ar = 1:9). This graphene showed relatively high content of nitrogen (∼2.3 %) and it is characterized by somewhat higher amount of defects when compared with the previous graphene sample. Regarding C 1s line, 75.8 % is sp^2 carbon,

11.7 % is sp^2 C-N bonds and the rest is a superposition of hydrocarbons and sp^3 C-N bonds. In spite of the increased amount of defects which should increase SEY (sp^3 contribution is higher) this material shows the best results. This unexpected result, which is out of the general scope of this research, is an illustration of the complexity of secondary electron emission process, and how simple correlations between the electronic structure and SEY cannot be established.

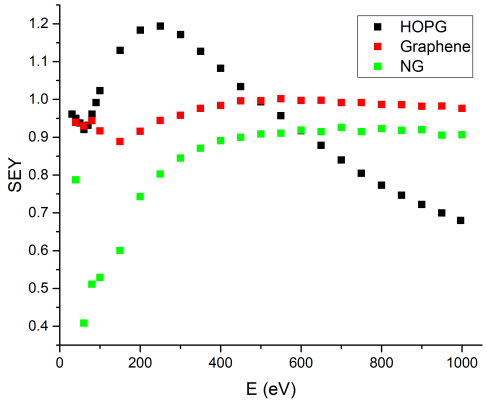

Figure 4.3: SEY curves of HOPG, graphene and N-doped graphene.

4.1 Substrates' analysis

In this section, the two materials chosen as substrates are analyzed and measured in order to follow the modification of electron emission properties with the deposition of a different material.

As seen in figure 4.4,maximum SEY of copper, 2, is slightly lower than the one of stainless steel, 2.15. These values are used as references to realize how much the SEY needs to be reduced. These metals have a high SEY due to the oxides present at their surface. The shape of the both SEY curves is very similar to the theoretical one (Figure 2.2), suggesting that the samples can be considered as rather flat.

In table 4.2, the surface composition for each material is presented.

Table 4.2: Surface composition of used substrates.

Substrate	C	O	Cr	Fe	Cu
Cu	55.8 %	35,9 %	-	-	8.3 %
SS	45.4 %	47.2 %	2.5 %	4.9 %	-

It can be seen that both materials are completely covered by oxides and hydrocarbons, since just a minor part of their surface composition is related to the material itself, and they are composed majorly of carbon and oxygen.

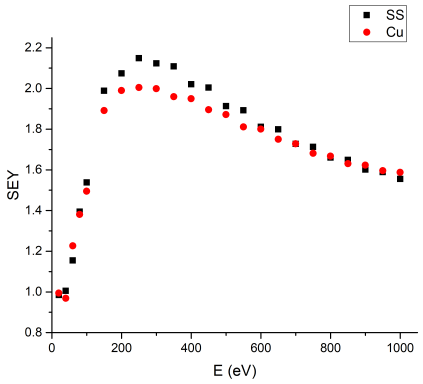

Figure 4.4: SEY curves of SS and Cu subs.

Regarding the copper sample, the main copper photoelectron line, Cu $2p_{3/2}$, has a complex shape, clearly indicating presence of more than a single phase (Figure 4.5). The position of the main peak at ∼932.5 eV can be attributed to metallic copper, but also to Cu_2O. Extended tail in a form of hump at about ∼935 eV, as well the minor satellite around 940-945 eV imply presence of a compound in which copper is present in Cu(I) oxidation state. By comparing the fitting models for different copper compounds, the best result was achieved for the superposition of Cu_2O (∼66 %) and $Cu(OH)_2$ (33 %). This can be confirmed by the modified Auger parameter which is 1950, an average value of Cu(I) oxide (1849.17) and Cu(II) hydroxide (1850.92) [46]. O 1s line also provides confirmation on the matter, since it can be fitted to three contributions situated at 530.8 eV (20.4 %), 531.5 eV (48.8 %) and 532.7 eV (30.8 %). These three contributions can be readily attributed to Cu_2O, $Cu(OH)_2$ [46] and oxidized hydrocarbons [40], respectively.

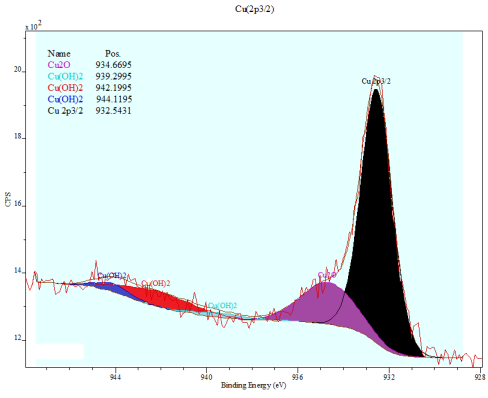

Figure 4.5: Cu $2p_{3/2}$ line fitting.

Concerning stainless steel, its O 1s line can be fitted to 2 contributions. The one at ∼530 eV (40 %) can be attributed to Cr and Fe oxidized states [47], while the one at 533.6 eV (60 %) is related to oxidized hydrocarbons [40]. As for the second contribution, we stress that the equivalent conclusion was obtained from fitting the C 1s line. The main lines of

iron and chromium (Fe $2p_{3/2}$ and Cr $2p_{3/2}$) are both subjected to the multiplet splitting effect when the elements are in the oxidized states. Therefore, their complex shapes had to be fitted by a set of symmetric peaks with well-defined constraints taken from [47]. With Cr $2p_{3/2}$ line fitting (Picture 4.6(a)), chromium is present at the surface in its Cr(III) oxide state (Cr_2O_3). On the other hand, a minor part of iron can be seen in its metallic state, 8 %, while the other 92 % of the Fe $2p_{3/2}$ line (Figure 4.6(b)) is iron in Fe(II) oxidized state (FeO). From this result it appears that the stainless steel surface is covered with the mixture of Cr and Fe oxides, and a layer of hydrocarbon contaminants on the top.

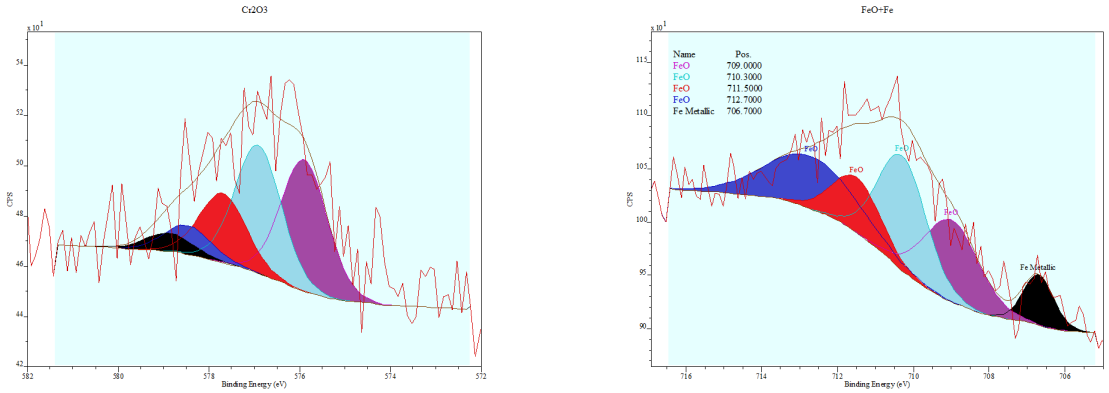

(a) Cr $2p_{3/2}$ (b) Fe $2p3/2$

Figure 4.6: Cr $2p_{3/2}$ and Fe $2p_{3/2}$ lines fitting.

4.2 Choice of the counter electrode

As explained in section 3.1, gold is one of the most inert materials for electrochemical processes. For that reason, all the experiments done throughout this work were done with a Au counter electrode. But, in order to verify this fact, other materials for the counter electrode were tested, namely, copper and stainless steel.

Firstly, with a copper electrode, the technique was not even possible to be performed. Acidic solutions are often used to etch Cu and electroplating is usually performed this way [48], using acidic electrolytes with copper counter electrode as a source of copper for coating. This way, while etching the Cu electrode, copper particles would mix with graphene in the solution, preventing this to be attached to the substrate. It is unknown why Cu ions prevent graphene flakes from being deposited, but visually and though XPS analysis it is confirmed that they have a big influence on the deposition. From this experiment, it was concluded that Cu electrode can not be used since it was not even possible to coat the substrate with graphene. So, stainless steel was used as a replacement for gold. Two different coatings were made, each one with a different counter electrode, in order to compare them. When using a Au electrode, a stainless steel substrate was chosen while with a SS electrode a copper substrate was used. Both samples were 1 hour depositions, with 20 V between electrodes and using 20 μL of HCl in the solution.

Figure 4.7 shows the differences between both C 1s lines and surface compositions of both samples are presented in table 4.3.

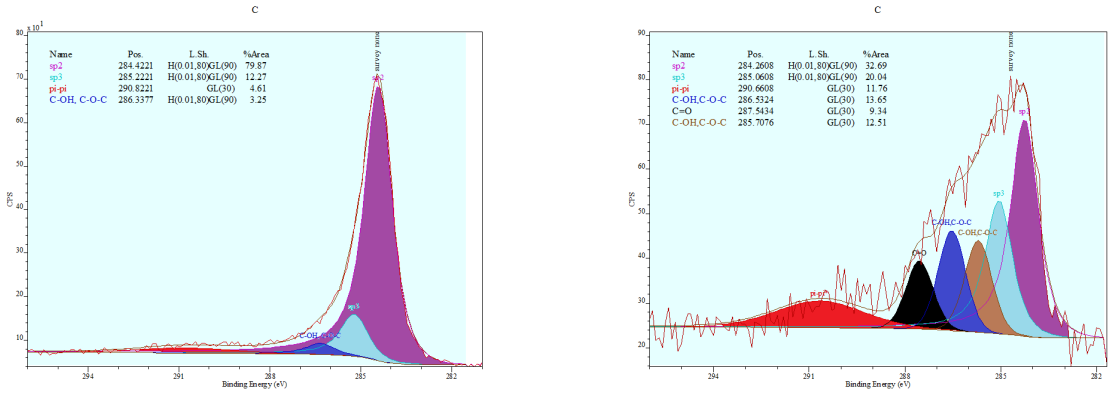

(a) Gold (b) Stainless steel

Figure 4.7: Carbon 1s line using Au and SS as counter electrodes.

Table 4.3: Composition analysis of the material deposited on SS using Au and SS as counter electrodes.

Counter electrode	C	O	Cr	Fe	Ni	Au
Au	92.6 %	6.1 %	1.1 %	-	-	0.2 %
SS	50.1 %	39 %	7.3 %	2.6 %	1 %	-

Looking at their XPS data, the differences are quite significant. The SS sample has only 50.1 % of carbon, and only a minor part of it is sp^2 related, and the major contribution for C 1s line fitting is related to the hydrocarbon bonds. Meanwhile, Au sample has more than 90 % of carbon. A major part of it is sp^2 carbon, and only 4.6 % is related to hydrocarbons. The amount of oxygen in the SS sample is also considerable, which is coherent with the C 1s line fitting. In the case of this line, the hydrocarbon contribution at 286.3 eV and different C-O contributions were fitted with a standard symmetric line shape (GL(30)), instead of an asymmetric one (H(0.01,80)GL(90)), due to the low amount of the sp^2 contribution.

Table 4.4: sp_2 and sp_3 ratio using Au and SS electrodes. HC stands for hydrocarbon and different C-O bonds.

Counter electrode	sp^2	sp^3	HC
Au	80 %	12.3 %	4.6 %
SS	34 %	20 %	37.5 %

The Au sample has a very low amount of contaminants, which together make only 7.4 % of the surface composition, including mainly oxygen, Cr (Cr_2O_3) and Au. Au is not completely inert to the process since a small amount of it is detected on the sample's surface. However, the most important conclusion is that the sp^2:sp^3 intensity ratio is even better than the one in the reference graphene sample, clearly illustrating that the transfer of free standing graphene from the suspension to the deposit was performed successfully.

On the other hand, approximately half (49.9 %) of the surface of the SS sample is composed of contaminants (O, Cr, Fe and Ni). Detailed fitting of the Cr $2p_{3/2}$, Fe $2p_{3/2}$ and Ni $2p_{3/2}$ line reveal that chromium and iron are present at the surface as Cr_2O_3 and Fe_2O_3, while Ni is even found in its metallic state. When compared to the SS substrate, Cr oxidized state is maintained while metallic Fe is no longer seen and FeO is transformed into Fe(III) oxide. Increased amount of Cr and Fe with respect to the SS substrate, and in particular observation of Ni at the surface, undoubtedly show that stainless steel counter electrode is etched similarly to the copper electrode. The metallic ions are then being co-deposited with graphene onto the substrate. Besides the increased contamination of the deposit even more dramatic result is observed from the C 1s line fitting: carbon is mainly present in the form of saturated hydrocarbons and molecules containing different C-O bonds. Under these conditions, free-standing graphene was transformed into a complex structure dominated by partially oxidized hydrocarbons and other sp^3 structures. Despite the SS sample having a completely different surface composition from the Au sample, filled with defects and contaminants, their SEYs are practically identical (Figure 4.8).

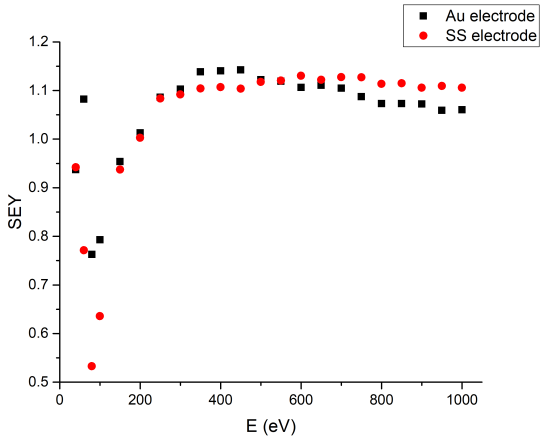

Figure 4.8: SEY curves for Au and SS as counter electrodes.

Coating with a SS electrode resulted in a completely different surface but led to a similar SEY (1.13) compared to the one obtained by the Au electrode (1.14). Other experiments were performed with both electrodes, namely prolonging time of deposition, and SEY results are still identical. Apparently, contaminants and other kinds of carbon besides sp^2, also lead to a decreasing of a material's SEY. Of course, one should bare in mind eventual differences in surface morphology of the two samples. Despite identical results, gold was chosen for counter electrode in order to preserve graphene original structure and morphology and to keep the surface with the minimum amount of contaminants possible.

4.3 Tuning the deposition parameters

In order to tune the parameters for the best possible usage of the technique (EPD), some experiments were made. Voltage and time of deposition were studied as well as the amount of HCl in the electrolyte.

To find a suitable deposition time for EPD experiments, different samples were made with different times, to study the influence of time in the coating process, surface composition and SEY. A stainless steel substrate and a gold counter electrode were used, and all the parameters voltage (20 V) and amount of HCl (20 μL), besides the time of deposition, were fixed. In that sense, five samples were made, with the deposition time of 15, 30, 60 and 90 minutes.

The 15 min sample is characterized with the lowest amount of carbon (83 %) and the largest amount of oxygen (11.2 %). This sample is the only one with iron present in its composition (1.3 %), since graphene is probably not continuous, it is still possible to have holes so that a signal from the substrate is detected. Concerning the O 1s line for this sample, 83.4 % are hydrocarbons (C=O and C-O-C) and 16.6 % are related to Cr and Fe oxidized states at 530.4 eV [47] (Figure 4.9(a)). These last two elements are found as Cr_2O_3 and Fe_2O_3 by fitting Cr $2p_{3/2}$ and Fe $2p_{3/2}$ lines accordingly. Again, when compared with pristine stainless steel surface, Cr(III) oxide was already present in the substrate, but Fe changed from a mixture of metallic Fe and FeO to Fe(III) oxidized state.

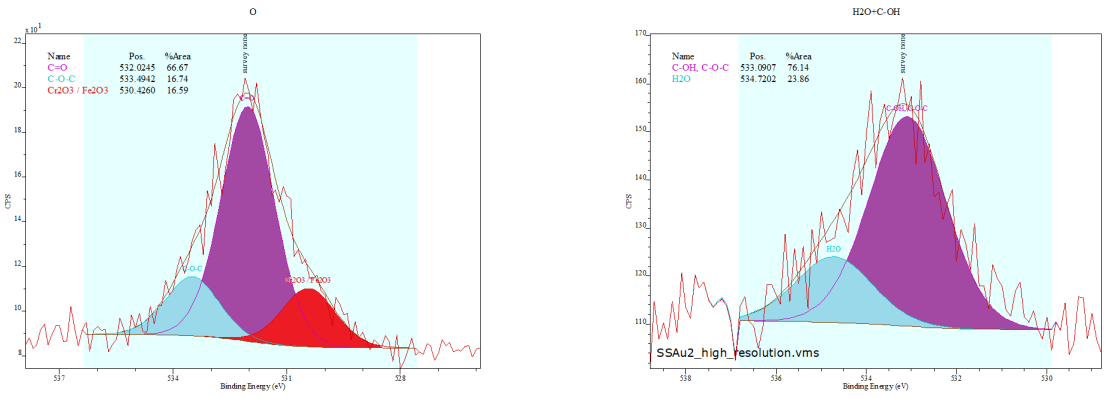

(a) 15 minutes (b) 90 minutes

Figure 4.9: Oxygen 1s line of the 15 and 90 minutes.

Samples with 30 minutes and 1 hour deposition times are very similar in their surface composition, with an average of 93 %, 6 % and 1 % of C, O and Cr (Cr_2O_3) respectively. Due to the increasing amount of carbon, which screens the substrate, less Cr is detected which also results in less O bonded to the chromium, consequently leading to a decreasing in the amount of oxygen. From 90 minutes on, Cr is not detected anymore leading to an increasing amount of carbon (95.4 %) and a slightly decrease in the amount of oxygen (4.3 %). Despite gold is not detected in the 15 min sample, its amount is constant (0.2 %) for

the rest of the samples.

Concerning sp^2 and sp^3 contributions in C 1s line, for 15 and 30 minutes depositions, sp^2 peak grows from 71 % to 75 % respectively, and sp^3 peak also grows from 14 % to 15.4 % respectively. From 1 hour on depositions, sp^2 and sp^3 contributions saturate, coming to a maximum of 80 % and 13 %, respectively. This ratio is practically what is seen in pure graphene. Table 4.5 presents sp^2 and sp^3 ratio with the increase of the deposition time.

Table 4.5: sp^2 and sp^3 ratio according to deposition time.

Contribution	**Graphene**	**15 min**	**30 min**	**1h**	**1.5h**
sp^2	74.5 %	71.2 %	74.8 %	79.9 %	79 %
sp^3	18.5 %	14 %	15.4 %	12.2 %	14 %
HC	3 %	4.4 %	4.5 %	3.3 %	3 %

The other contributions for all C 1s lines are related to $\pi - \pi^*$ satellite and C-OH and C-O-C bonds. These hydrocarbons make ∼76 % of the O 1s line while the other 24 % are adsorbed water. Since Cr is no longer detected, there is no related contributions in the O 1s line (Figure 4.9(b)).

Regarding SEY, it is consistent with what should be expected. The increasing deposition time leads to an increase of the coating thickness, consequently resulting in a decreasing of SEY. The thickness of the 90 minutes sample was estimated in ∼20 μm using SEM. The sample was tilted into a 70° angle and using simple trigonometry, the thickness of the coating was estimated (Figure 4.10).

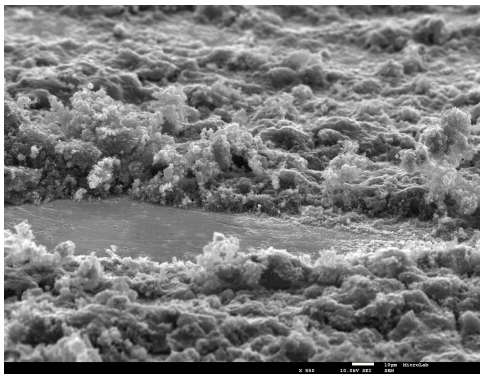

Figure 4.10: SEM image of 90 minutes sample from which the thickness was estimated.

Looking at figure 4.11, it is possible to see that SEY gradually decreases with the deposition time, going from 1.46 for 15 min deposition to the reference value, ∼1, for 90 minutes deposition. For a 15 minutes deposition, the shape of the curve is still similar to the shape of a flat surface, also identical to bare stainless steel, and with the increase of deposition time it becomes recognizable to a rough surface. So, the best achieved results such in SEY as XPS was the 90 minutes deposition, since it was the one with the lowest SEY and the highest amount of graphene in its original state (high amount of sp^2 carbon)

with no contaminants besides oxygen. Although the surface composition practically saturated after 30 minutes and the sp^2:sp^3 contribution ratio did not change after 1 hour of deposition, it is clearly observed the gradual drop of SEY and change of the shape. The latter reveals that the drop of SEY is mainly a consequence of the surface morphology modification.

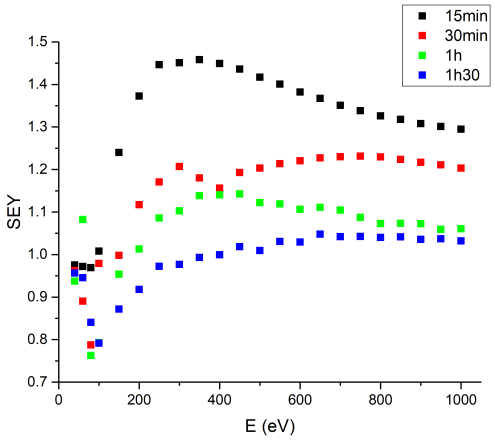

Figure 4.11: SEY curves as function of time of deposition.

SEY was studied as a function of the deposition voltage to see its influence on SEY as well as on the composition. In that sense, a 60 volt power supply was used and five different voltage values were tested (20, 30, 40, 50 and 60 V). Increasing the voltage leads to higher currents in the solution (higher ion mobility), resulting in higher deposition rates. This study was also performed in a stainless substrate with a gold counter electrode. All other parameters, besides the deposition voltage, were fixed: deposition time (15 min) and amount of HCl (20 μL). Taking a closer look at table 4.6, it is possible to follow in detail the surface composition as a function of the deposition voltage.

Table 4.6: Table of elemental composition for different deposition voltages.

Element	**20 V**	**30 V**	**40 V**	**50 V**	**60 V**
C	82.9 %	79.2 %	64 %	89.6 %	89.1 %
O	11.2 %	12.4 %	30 %	8.2 %	7.8 %
Cl	3.4 %	5.4 %	-	1 %	1.9 %
Cr	1.2 %	1.3 %	5.6 %	1.2 %	1.1 %
Fe	1.3 %	1.4 %	-	-	-
Au	-	0.3 %	0.4 %	-	0.1 %

It seems that 40 V is the turning point for most of the contributions, which can be the maximum and the minimum for most of the elements. Besides Cl, that have quite a puzzling behavior through the increasing voltage, C, O, Cr and Au behave quite similarly but symmetrically. In the case of Fe, it is present for 20 and 30 V, which means that the

surface is not completely covered or the coating is not thick enough for XPS not being able to detect it, since Fe is characteristic of the SS substrate. Results of the C 1s line fitting for all the samples are summarize in table 4.7. Carbon has its lower surface contribution at 40 V (64 %) and that is coherent through C 1s line fitting, where its sp^2 contribution is the lowest with only ∼60 % while sp^3 is the highest, with 20 %. The other 20 % of C are related to oxygen bonds (C-OH, C-O-C and C=O) which makes sense since O contribution is maximum at 40 V. It also appears that the fraction of sp^2 contribution is the highest for the 50 V and 60 V, and the lowest for 20 V.

Table 4.7: C 1s fitting for different deposition voltages.

Contribution	**20 V**	**30 V**	**40 V**	**50 V**	**60 V**
sp^2	71.2 %	75.8 %	59.2 %	84 %	83 %
sp^3	14 %	17.7 %	20.2 %	9.4 %	11.5 %
HC	4.4 %	5.6 %	18.2 %	4.7 %	3.8 %

Chromium also has its maximum contribution at this same voltage which originates some Cr hydroxide ($Cr(OH)_3$) and oxide (Cr_2O_3) bonds that can be identified through the proper fitting of both O 1s and Cr $2p_{3/2}$ lines. The results in table 4.8 are consistent with O 1s lines fitting.

Table 4.8: Cr $2p_{3/2}$ fitting for different deposition voltages.

Contribution	**20 V**	**30 V**	**40 V**	**50 V**	**60 V**
Cr_2O_3	100 %	100 %	95 %	87 %	80 %
$Cr(OH)_3$	-	-	5 %	13 %	20 %

C, O and Cr have a similar behavior in the sense that they behave symmetrically regarding the 40 V value (symmetry point), in which C decreases until that point and then increases, and O and Cr behave the opposite way. Usually the amount of a deposit increases with increasing the voltage, but more uniform films are produced at more moderate potentials [24]. So 40 V is the voltage at which the carbon contribution is the lowest and contaminants contributions (O and Cr) are the highest, and still, it is the sample with the lowest SEY of the five, 1.24 (Figure 4.12). At the same time, the sample obtained with 60 V, which should have the highest carbon content and the highest sp^2 contribution, has largest SEY. This is another indication that tailoring parameters which will provide low SEY is far from straight forward.

As it can be seen from figure 4.12, SEY decreases from 1.45 to 1.24, from 20 to 40 V respectively, and then increases to 1.5 at 60 V. SEY values for 20 and 60 V, and for 30 and 50 V are very similar, so SEY as a function of deposition voltage can be almost symmetrically described.

In the surface morphology of the 40 V sample observed in the SEM images (Figure 4.13), it is also possible to distinguish between sp^2 carbon and, according to [6], what can be some kind of 3D amorphous carbon nanostructure in the form of bright spots in the

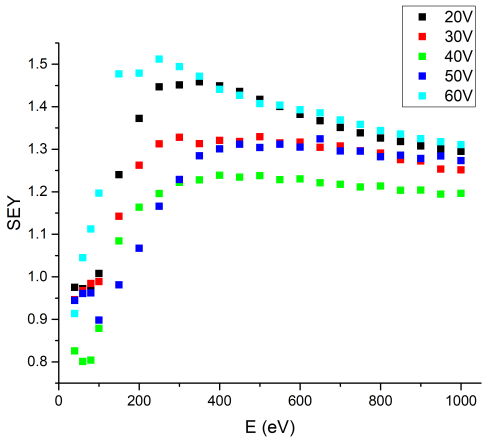

Figure 4.12: SEY curves as function of voltage of deposition.

low magnification image. Their 3D structure is revealed only in the high magnification images, such as figure 4.13(b).

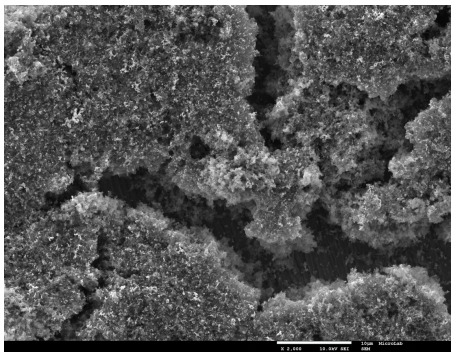

(a) Low magnification

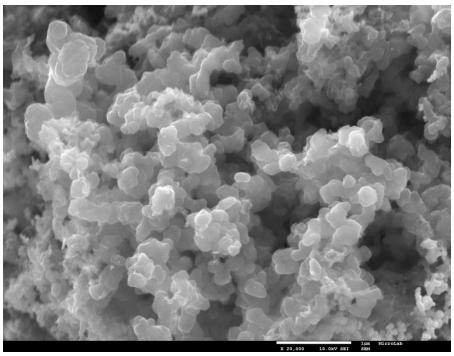

(b) 3D carbon

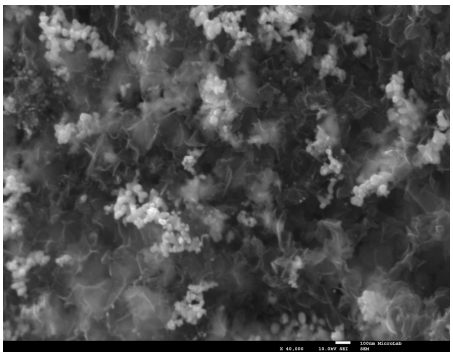

(c) sp2+sp3

Figure 4.13: SEM images for 40 V deposition sample.

EDS analysis revealed that these structures contain only carbon. The fact that such

3D structures can be formed only by sp^3 hybridized carbon is consistent with the XPS results which show that 40 V sample has the highest sp^3 relative content. In the last image (Figure 4.13(c)), it is possible to see a mixture of sp^2 carbon and amorphous carbon defects, where graphene structures can be recognized from figure 4.1. Since the presence of non-conductive sp^3 carbon should not reduce the electron yield, lower SEY is probably related to the highly corrugated morphology of these structures.

A final experiment was done regarding the HCl amount in the solution. The amount of HCl was previously determined (20 μL) but there was the necessity to know what would occur in terms of composition, SEY and even morphology, if there would be HCl in excess. For this purpose, 150 μL were added to IPA and a deposition of one hour was performed onto a copper substrate.

Even after one hour of deposition, it is still possible to detect 6% of Cu on the surface. Carbon is the major contribution, with 83.9%, and a very low amount of oxygen is detected, 3.3%. It seems that deposition voltage is not the only factor that increases the etching of electrodes, since in this case 6.8% of Au is detected on the surface. Voltage increases ion mobility, resulting in the increase of deposition current, but the effect is also achievable by the increase of HCl which increases the ion density in the solution. This increase in the amount of Au is also clearly verified through SEM images (Figure 4.14), where golden nanoparticles were observed (Figure 4.14(b)) and identified using Energy Dispersive Spectroscopy (EDS) (Figure 4.15). The amount of gold in the sample also may increase its SEY, which now reaches maximum value of $\sim$1.3.

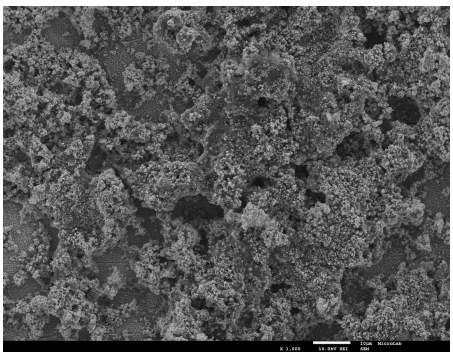

(a) Low magnification

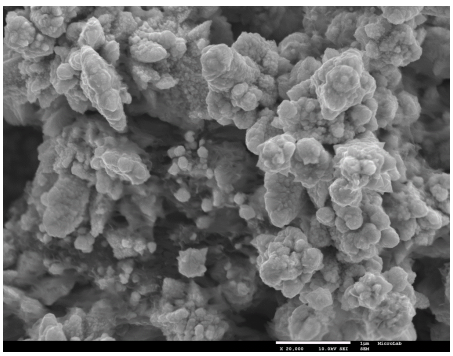

(b) High magnification

Figure 4.14: SEM images of the sample produced with HCl in excess.

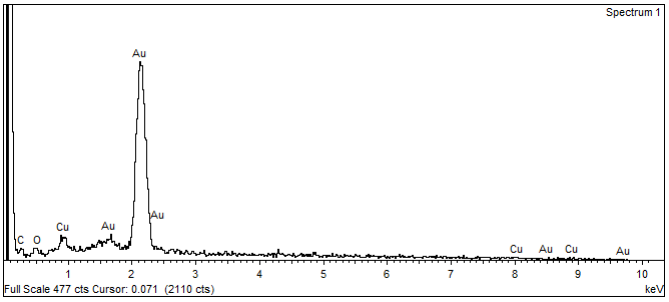

Figure 4.15: EDS measurement of gold nanoparticles present in figure 4.14(b).

4.4 SEY results of samples obtained with optimized deposition parameters

Among all the produced coatings and experiments made, three different samples were able to reach what was considered the reference value for SEY (∼1). Each sample is a different combination between substrate and counter electrode: SS substrate and gold electrode (SSAu), Cu substrate and also Au electrode (CuAu) and Cu substrate with SS electrode (CuSS). The three coatings were produced with the same moderate voltage (20 V) and the same amount of HCl (20 μL). The only difference in EPD parameters is the deposition time, where SSAu, CuSS and CuAu are 90, 60 and 30 minutes deposits, respectivel.

Concerning XPS data, table 4.9 shows the surface composition of the three samples. SSAu and CuAu have similar compositions, where carbon contribution is relatively the same, and SSAu, despite a higher oxygen amount, gold percentage is lower than CuAu. CuAu also has a Cu contribution from the substrate. Detailed fitting of the Cu $2p_{3/2}$ line shown in figure 4.16 revealed that copper exists in its metallic state (54.7 %) whilst 44.3 % of copper is present as $Cu(OH)_2$. Modified Auger parameter has value of 1850.5 eV thus confirming the presence of these compounds [46].

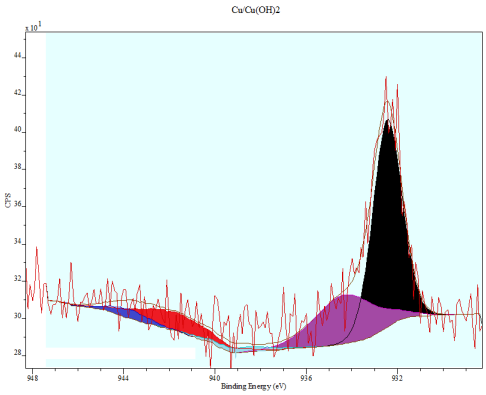

Figure 4.16: Cu $2p_{3/2}$ fitting of the CuAu sample.

C 1s line fitting of SSAu sample reveals 79 % and 14.2 % of sp^2 and sp^3 carbon, while

only 3 % are in the form of C-OH and C-O-C bonds. This low amount of saturated hydrocarbons can be confirmed from the O 1s line, where their contribution is 76 % and the other 24 % is adsorbed water. Looking at CuAu C 1s line, 79 % is sp^2 carbon, 12.5 % is sp^3 and 4 % are saturated hydrocarbons. These C-OH and C-O-C bonds are confirmed in O 1s line, which they make 29.5 % of it and the others 70.5 % are metallic oxygen (bound to copper). Despite some small differences in contaminants between these two samples, when looking at both carbon amounts and C 1s lines, they are identical.

Table 4.9: Composition table of the three samples with the lowest SEY.

Sample	C	O	Cr	Fe	Cu	Au
SSAu	95.4 %	4.3 %	-	-	-	0.3 %
CuAu	95.3 %	2.8 %	-	-	1.4 %	0.5 %
CuSS	54.2 %	40.1 %	4.4 %	1.3 %	-	-

Trying to correlate XPS data with SEY, since XPS spectra of SSAu and CuAu samples are similar, their SEY should be identical. That was confirmed with their SEY measurement where they got exactly the same result, 1.04 (Figure 4.17). It is important to point out that CuAu sample was able to get identical results with just half of the deposition time of SSAu.

Concerning CuSS sample in terms of surface composition, it is completely different from the other two samples. These results were already expected from the previous results in section 4.3. This sample has a considerably low amount of carbon and high amount of oxygen when compared to the other two. From the XPS analysis of the Cr $2p_{3/2}$ and Fe $2p_{3/2}$ lines, Cr and Fe are also detected in an oxidized state, Cr_2O_3 and Fe_2O_3, respectively. These two compounds make 55.5 % of the O 1s line, while the rest 44.5 % are related to organic bonds to carbon. C 1s line fitting shows that only 13 % of it is sp^2 carbon, while 23.2 % is sp^3 carbon and 49.2 % are different types of C-O bonds (25.1 % - C-OH and C-O-C, 18.5 % - C=O, 5.6 % - O-C=O). Note that all the percentages missing in C 1s line contributions are related to the $\pi - \pi^*$ satellite, which is not being mentioned.

Although CuSS sample surface composition is completely different from the other two, and sp^2 contribution is extremely low, its SEY is similar to the other two samples, 1, which can be seen in figure 4.17. It seems that graphene does not have to maintain its structure and have low contributions of sp^3 carbon or contaminants, in order to decrease SEY. With SEM images of the three samples (Figure 4.18), sp^2 carbon and 3D carbon structures can easily be distinguished. Since SSAu and CuAu samples are practically identical, only one SEM image of each was presented. Figure 4.18(a) is a low magnification image of the SSAu sample, where small parts of the substrate can be seen and the deposited coating can be described as rough and far from uniform, while figure 4.18(b) is a high resolution of CuAu sample, in which graphene structures can be seen. Despite graphene predominating the entire surface, sp^3 structures as in figure 4.13(b) are also present.

From the low resolution point of view (Figure 4.18(c)), CuSS deposit is a bit similar to the other two, although the non uniformity in the form of deep cracks prevails. But,

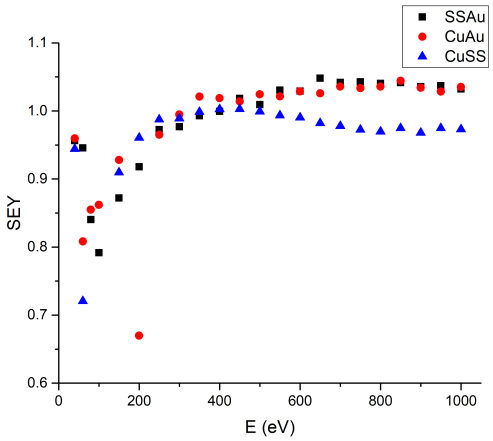

Figure 4.17: SEY curves of the three lowest SEY samples.

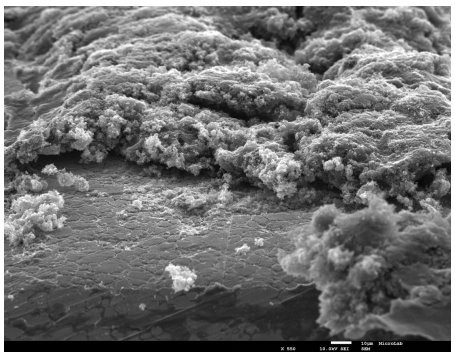

(a) SSAu

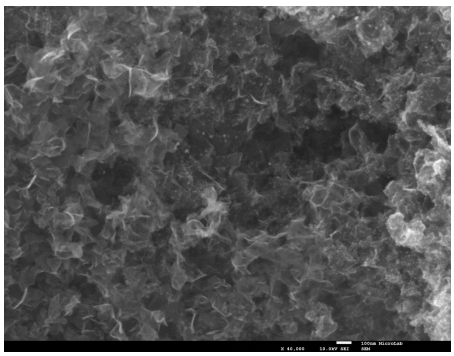

(b) CuAu

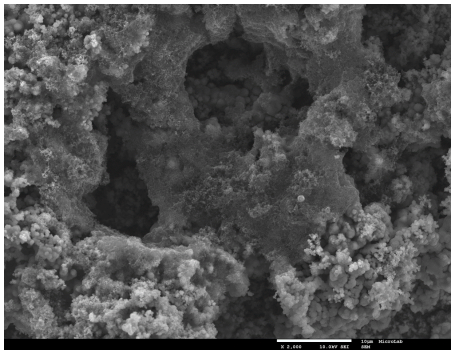

(c) CuSS - Low magnification

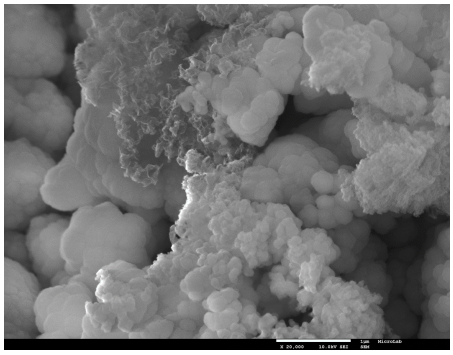

(d) CuSS - High magnification

Figure 4.18: SEM images of SSAu, CuAu and CuSS samples.

when looking at figure 4.18(d), completely different structures, which predominate the surface, can be seen. These structures are quite different from the ones identified as sp^3 carbon in figure 4.13(b) but still might be considered as sp^3 structures since there is an immense amount of sp^3 carbon (and hydrocarbons) in XPS spectra. Besides, sp^2 structures are 2D and these are clearly 3D nanocrystal-like structures. These were also confirmed as being carbon through an EDS measurement. Some graphene can also be seen among these

structures, which is consistent with the XPS data. It seems that when using a stainless steel electrode, graphene completely looses its morphology and transforms itself into more complex tridimensional structures. There is a transformation of graphene (sp^2) into some sp^3-based compounds, in which chemical bonds are completely transformed. Probably, Cr in its present form (Cr_2O_3 nanoparticles) seems to be a catalyst for this chemical transformation. Nevertheless, despite graphene loosing its morphology and composition, the appearance of these completely different carbon structures and a surface full of contaminants, is still capable to reduce SEY down to $\sim$1.

In order to verify if these graphene coatings were stable, two tests were performed: exposure to atmosphere and baking. An SSAu type of sample was left exposed to air during approximately one month, and XPS and SEY measurements were repeated. Surprisingly, the amount of carbon slightly increased ($\sim$1 %) while oxygen decreased 0.7 % in the tested sample. This slight increase in carbon resulted in a decrease of the sp^2 peak from 84.1 % to 79.9 %, and a 1 % increase in sp^3 contribution. Since oxygen went down, saturated hydrocarbons (C-OH and C-O-C) decreased from 3.3 % to 0.9 %. This can also be confirmed from the O 1s line. The fact that the amount of carbon increased but sp^2 contribution decreased, means that hydrocarbons from air are adsorbed as contaminants. This extra layer of hydrocarbons led to an increase of $\sim$0.1 in the SEY of the sample.

Three different samples (SSAu, CuAu and a different CuSS type sample (CuSS*)) were submitted to a 150 $^{\circ}C$ baking for approximately 64 hours at low 10^{-7} mbar. This experiment studies the accumulative effect of air exposure and baking since all the samples were previously exposed to the atmosphere for approximately 1 month before being submitted to baking.

Comparing directly SSAu and CuAu samples, since they are similar, small differences can be verified regarding XPS. In both samples, there is a slight decrease and increase of carbon and oxygen contribution, respectively. In the case of SSAu, gold decreases while in CuAu this element is no longer detected, probably due to being covered with external contamination. Still on CuAu, the amount of Cu also decreases due to higher O amount, which is consistent with the previous statement. Concerning sp^2 and sp^3 carbon ratio in both samples, it is maintained after baking experiments but hydrocarbon contribution increases in the C 1s line. In the case of the CuSS* sample, carbon percentage is also slightly lower while oxygen increased more when compared to the other two samples. This resulted in an increasing of C-O contributions (C-OH and C=O) in C and O 1s lines, while sp^2 and sp^3 carbon ratio is maintained. Table 4.10 resumes the differences in surface composition between before and after baking measurements of all three samples. Looking at SSAu, CuAu and CuSS* samples, their SEY increased in 0.1, 0.1 and 0.2 respectively.

The increase of Cr in the case of CuSS* can possibly be explained by the removal of carbon from the areas where carbon is in very thin layer covering the SS substrate. This

Table 4.10: Surface composition of SSAu, CuAu and CuSS* relative to before baking measurements.

Sample	$-\Delta$**C**	$+\Delta$**O**	$+\Delta$**Cr**	$-\Delta$**Cu**	$-\Delta$**Au**
SSAu	1.3 %	1.4 %	-	-	0.1 %
CuAu	1.5 %	2.6 %	-	0.4 %	0.5 %
CuSS*	2.1 %	3.3 %	2.4 %	-	-

would explain increase of Cr in this sample, where in some areas it might have a thin layer of carbon covering Cr-oxide nanoparticles. When baking, carbon can be removed, therefore, opening Cr-oxide surface.

From the air exposure experiment, it was seen an increase of SEY in $\sim$0.1. When the three different samples were submitted to baking after also 1 month of air exposure, the same increase in SEY of $\sim$0.1 was checked. For this reason, it can be concluded that this increase in SEY is due to the air exposure and not to the baking.

4.5 Ageing of electrodes

During the process of EPD, some chemical reactions occur at the counter electrode, namely etching, as already explained. When using stainless steel plate as a counter electrode, pitting (see section 2.2.1) is observed. Tiny holes can be clearly seen with bare eye at the surface of the electrode and from the optical microscope images (Figure 4.19) it is possible to estimate the size of the pits. Their diameter is variable but the largest ones observed were estimated to $\sim$100 μm.

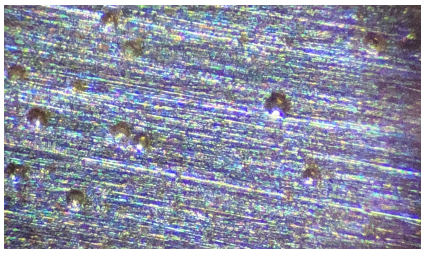

Figure 4.19: Picture of pitting effect on stainless steel electrode.

Chromium is the most abundant element at the surface of stainless steel, while iron and nickel are elements more present at the bulk. Through pitting effect, it is now possible to understand from where Fe and Ni contaminations previously detected with XPS in the deposit (see Section 4.2) originate from. Iron and nickel are only detected when a SS counter electrode is used, while Cr can be also detected with Au counter electrode, since its source can be the SS substrate itself.

While in stainless steel the corrosion is localized, in the case of gold, the entire electrode is uniformly etched. That fact is nicely correlated with XPS data of most of the samples

produced with Au electrode, where this element is detected. Table 4.11 presents the surface composition of the gold electrode before and after EPD, and huge differences can be verified. Before the EPD, the gold electrode is thoroughly cleaned and still it is full of saturated hydrocarbons. From C 1s line, ∼21.5 % are C-C bonds while 60.8 % and 17.7 % are C-OH/C-O-C and C=O bonds, respectively. This is consistent with O 1s fitting, revealing that 16 % is bound as adsorbed water and the other 84 % match to oxidized hydrocarbons.

Table 4.11: Surface composition of Au electrode before and after EPD.

	C	**Cl**	**O**	**Au**
Before	41 %	-	32 %	27 %
After	81.6 %	11.8 %	3.4 %	3.2 %

The surface composition of Au after the EPD is completely different from the previous one. Firstly, the amount of oxygen is drastically reduced, as well as of gold. There is a considerable amount of Cl contribution. Cl $2p_{3/2}$ is found at 198.1 eV and Au $4f_{7/2}$ is situated at 86.5 eV, and with Cl 2p and Au 4f lines fitting, gold chloride (AuCl) is found at the surface [49]. Finally, the major difference is in the amount of carbon and C 1s line shape. Carbon contribution increased significantly and the C peak transformed from an organic shape to an asymmetric graphitic carbon C 1s line. This line was perfectly fitted to the peak model used for graphene or graphite, where 65 % and 26.4 % are the relative amounts of sp^2 and sp^3 carbon respectively, and only 4.7 % are C-OH and C-O-C bonds. Visually, the electrode ends up completely black, and with XPS data and SEM images (Figure 4.20), it can be determined that graphene or graphite (depending on the used suspension) is also being deposited on the counter electrode and not only on the substrate.

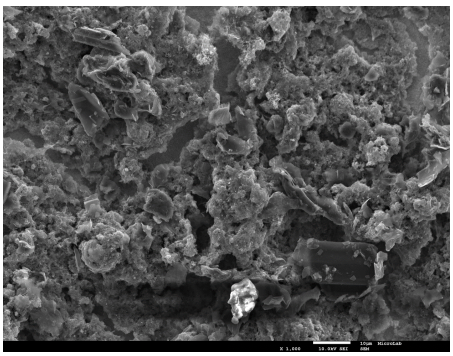

(a) Low magnification

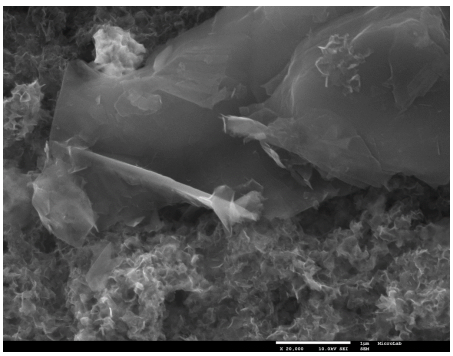

(b) High magnification

Figure 4.20: SEM images of the Au electrode after EPD of graphene and graphite.

As it will be showed in section 4.7, EPD of graphite particles has been also performed. Figure 4.20 shows the SEM images of the gold electrode after a few EPD processes of both graphene and graphite. Stacks of graphite from 5 to ∼20 μm can be readily observed at the surface (Figure 4.20(a)) as well as graphene structures among them (Figure 4.20(b)).

XPS and SEM analysis of the Au electrode show that graphene and graphite particles are also deposited on the counter electrode and maintain their original morphology, composition and electronic structure. While majority of graphene and graphite particles charge positively in the suspension prepared for EPD, this is a strong indication that some of the particles also charge negatively. Therefore, the deposition takes place on both electrodes, although at much lower rate on the Au counter electrode. It should be noted that this effect was not observed on the SS counter electrode.

4.6 Alternative 1 - CVD grown graphene

CVD grown graphene obtained from INL was also tested for the SEY reduction of a material (copper in this case). Since copper is one of the materials commonly used for accelerator tubes, direct CVD growth of graphene on the inner walls of copper tubes could have strong technological and commercial potential. This kind of graphene is typically one layer thick, as explained in section 2.1.3.2. The process itself is rather simple and better adhesion is expected as compared to EPD. At first sight, modest reduction in SEY, particularly for a multilayer coating was expected, since the electrons are typically originating from first several nanometers of the material. Results of SEY measurements of the uncoated (Bare Copper), single layer coated (Monolayer) and multilayer coated sample (Multilayer) are shown in figure 4.21. Contrary to the expectations, an excellent result for the single layer coating was obtained, while the multilayer coating is only slightly better than the uncoated sample. The shape of the curves are also confusing. Deposition of a single atomic layer cannot affect the surface morphology and consequently the shape of the SEY curve. This might happen eventually in the case of multilayer deposition. The experimental results of SEY measurements are exactly the opposite: the SEY curve shape of the multilayer sample follows that of the uncoated copper, whilst the shape of the Monolayer sample corresponds to highly corrugated surfaces. SEY maximum for the uncoated sample is typical for technical metal surfaces, usually covered with metallic oxides, moisture and other impurities.

In order to understand better the obtained results, XPS analysis of all three samples was performed. In almost all three samples, carbon, oxygen and copper were naturally observed. The results of the composition analysis are summarized in table 4.12.

Table 4.12: Composition analysis of CVD grown graphene samples.

Sample	C	O	Cu
Bare Cu	51.8 %	39.2 %	8.9 %
Single layer	72.6 %	27.4 %	-
Multilayer	55.3 %	25.8 %	18.9 %

Contrary to the expectations, although in accordance with the SEY measurements, copper is not observed in the single layer coated sample. This means that the amount of coating deposited is several nanometers thick, which explains significant drop of the

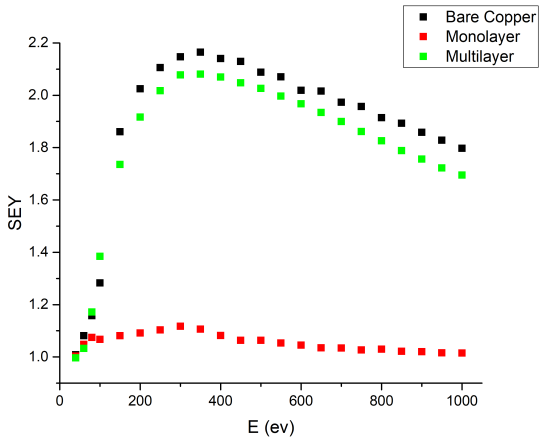

Figure 4.21: SEY curves for CVD grown graphene coatings.

secondary electron yield and significant modification of the SEY curve shape. Another peculiar thing is that there is a smaller amount of copper in the Bare Cu than in the Multilayer sample, which in turn, has the smallest amount of carbon.

In the case of the Bare Cu sample, copper is present at the surface in its metallic state (12 %) and as $Cu(OH)_2$ (88 %). This was concluded from the Cu $2p_{3/2}$ line and O 1s line fitting and further confirmed by checking the modified Auger parameter. Besides, from the C 1s and O 1s line fittings, saturated hydrocarbons (C-C and C-H bonds at the energy of 284.7 eV [50]), significant amount of C=O and some quantity of C-OH and C-O-C groups were detected. Interestingly, improved fit of the C 1s line is obtained when adding C sp^2 contribution, which is not expected (Figure 4.22(a)). The surface should be considered as metallic copper covered with two layers. The first layer is $Cu(OH)_2$ and then a layer of hydrocarbons on the top. Both layers are formed due to the exposure to the atmosphere.

Fit of the C 1s line taken from the Monolayer sample (which is certainly not the case as already discussed), is practically the same as in the case of the uncoated sample: there is ∼12 % of sp^2 carbon, ∼46 % of C-C and C-H bonds, 21 % of C-O bonds and ∼20 % of C=O bonds (Figure 4.22(b)). As for the O 1s line, it is also observed considerable amount of adsorbed water (23 %), and other lines fit are related to C=O. Any kind of Cu-O contribution is now not observed, in consistence with the absence of copper photoelectron lines in the survey. Clearly, a layer of hydrocarbons of a similar type as in the bare Cu are present at the surface, but of much larger thickness, thus being the reason why copper is no longer detected.

In the case of the multilayer sample, there is no copper in Cu(II) oxidation state. From the fitting, copper is present in the form of metallic Cu (∼60 %) and as Cu_2O (∼40 %), which is also supported by the O 1s line analysis. So the chemical treatment removed the hydroxide layer, and after this reduction Cu_2O is left behind. C 1s line analysis shows that

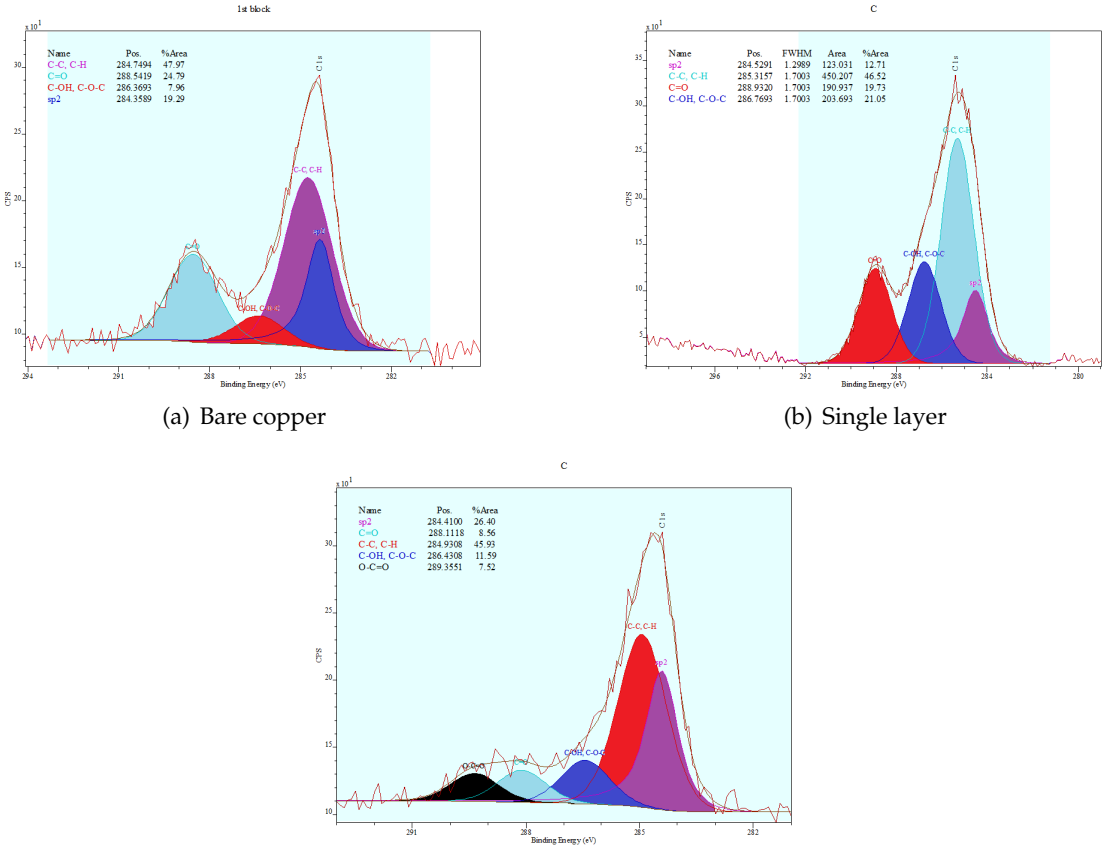

(a) Bare copper

(b) Single layer

(c) Multilayer

Figure 4.22: Carbon 1s line of CVD grown graphene samples.

the relative intensity of the sp^2 contribution is indeed higher than in other two samples. Other contributions are standard – C-C and C-H saturated hydrocarbons, C-OH and C-O-C bonds, C=O bond and COO bonds (Figure 4.22(c)).

Despite the largest relative amount of sp^2 carbon is indeed present in the Multilayer sample, the largest overall amount of carbon is the highest in Monolayer sample. The CVD process removes Cu-hydroxyl layer, although this cannot be confirmed for the single layer sample, in which the carbon based layer is too thick to observe copper. Namely this layer seems to be responsible for the SEY reduction.

Table 4.13: C 1s line contributions of CVD graphene samples.

Sample	sp^2	**C-C, C-H**	**C-O**	**C=O**
Bare Cu	19.2 %	48 %	8 %	24.8 %
Single layer	12.7 %	46.5 %	21 %	19.8 %
Multilayer	26.4 %	45.9 %	11.6 %	16.1 %

Last but not least, optical microscope images of the three surfaces with the magnification of about 200 were taken and are shown in figure 4.23. The orientation of samples

was always the same – the grooves of the copper sheets are vertically oriented. Probably graphene flakes of the polygonal form in the single layer sample are observed (Figure 4.23(b)) but usually not in the multilayer sample. The polygons in Multilayer sample were seen at one spot only (Figure 4.23(d)), which is why there are two images of this sample. Figure 4.23(c) is the typical one.

In conclusion, although CVD growth of graphene on copper seems like a very promising approach in reducing SEY, the analyzed samples do not fulfill the demands. Although the presence of sp^2 structures cannot be excluded, thickness, as well as the composition and detected bonds of the sample cannot be related to pure Mono or Multilayer graphene grown on copper surface. Reduced SEY was observed in, what is claimed to be, Monolayer sample. Nevertheless, this particular synthesis approach is most probably not suitable for SEY reduction in accelerators.

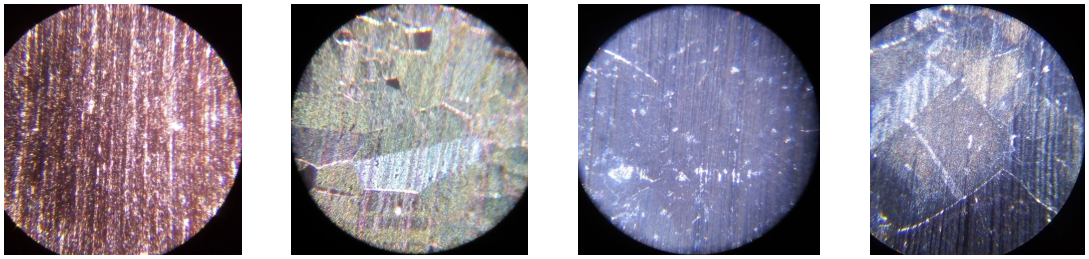

(a) Bare copper (b) Single layer (c) Multilayer (d) Multilayer

Figure 4.23: Optical microscope images of CVD graphene coated samples.

4.7 Alternative 2 - Graphite coating by EPD

As an alternative to graphene, tests with graphite were performed. The powder, acquired from REQUIMTE, is pyrolytic graphite being a waste of the high temperatures furnaces used in the metallurgy industry. The graphite powder was dispersed and deposited in exactly the same way as graphene in order to be able to compare them directly. So two samples, one of graphite and one of graphene, were produced with the same parameters. For this reason, EPD was performed during one hour, with 20 V and 20 μL of HCl. Since graphite particles are much heavier than those of graphene, it was needed to sonicate more often, every 10 minutes instead of 15, during the EPD.

XPS data shows that the surface is majorly composed of carbon (86.5 %) as expected, despite being a little bit lower than in the case of graphene (92.6 %). Looking more closely to C 1s line (Table 4.14), graphite has a higher amount of sp^2 carbon and less sp^3 bonds than the graphene sample.

This difference is normal since graphene has to be produced and defects come along with its production method, while graphite should be entirely composed of sp^2 carbon

Table 4.14: C 1s contributions for graphene and graphite samples.

Sample	sp^2	sp^3	**HC**
Graphene	78.8 %	12.5 %	3.2 %
Graphite	86.7 %	9.6 %	2.5 %

in its natural state. Differences can also be checked in the oxygen contribution, where graphite has 10.8 % and graphene has only 6.1 % of oxygen. Both samples have similar amounts of Cr and Au, but chlorine is present in the case of graphite. This suggests that graphite is more easily contaminated with Cl than graphene, despite this element being also present in some graphene samples.

Despite not being able to distinguish graphite and graphene through XPS spectra, these two allotropes of carbon have different SEYs (Figure 4.24) and morphology.

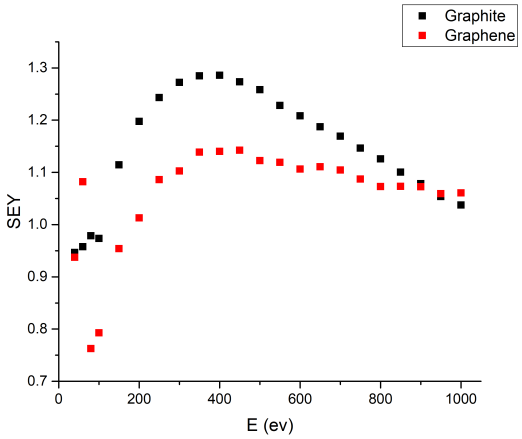

Figure 4.24: SEY curves of bare SS, graphite and graphene by EPD.

So, considering both samples were made with the same parameters, a difference of 0.15 in their SEYs can be verified, since SEY of graphene is 1.15 and SEY of graphite is 1.3. Despite their similar surface analysis with XPS, they are quite different in terms of secondary electron yield. In that sense, their structure and morphology plays a bigger role (Figure 4.25).

With SEM it is possible to clearly see the difference between graphene and graphite. While graphene has a highly irregular, disoriented and "paper-like" structure which have a maximum of 1μm in size, graphite has big stacks of highly oriented sheets of graphene that can go up to 20/30 μm which results in a more "rocky" morphology.

These results may be correlated with different shapes of SEY curves shown in figure 4.24. The shape of the curve in the case of graphite indicates that sample may be considered as flat. Although the morphology of the sample is rocky, the protrusions are much less efficient in recapturing secondary electrons than the paper-like structures of graphene.

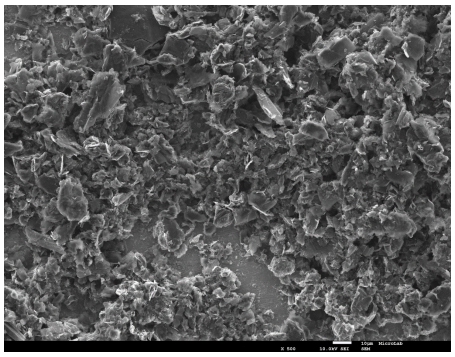

(a) Low magnification

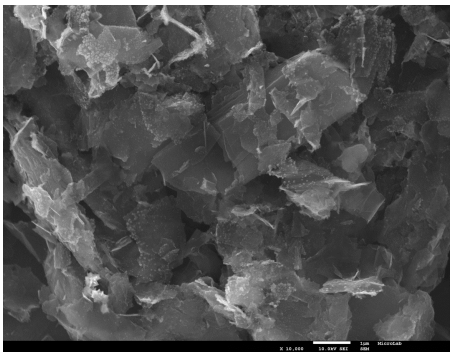

(b) High magnification

Figure 4.25: SEM images of graphite coating by EPD.

Another potential difference is in the number of graphene sheets in a stack. In the case of graphite we may consider this number to be infinite (with respect to the depth from which secondary electrons originate) whilst in the case of the free-standing graphene the number of layers in the platelet span from 10 to 20. According to [6] it appears that SEY of graphene increases with the number of layers in the platelet, which could also explain higher SEY from graphite particles compared to that of graphene.

4.8 Alternative 3 - Graphite spray

As the last alternative in this work, a commercial graphite based spray Graphit 33, produced by Kontakt Chemie, was purchased. This kind of products are often used to coat the electrodes of energy analyzers in order to reduce their SEY. In order to be measured and analyzed, a stainless steel plate was spray coated, resulting in a 150 μm thick coating. The thickness of the coating was measured with a micrometer (difference between the thickness of the substrate with and without the coating).

Although the spray is supposed to be graphite based, when compared directly with graphite (Section 4.7) via XPS spectra, they are quite different. Graphit 33 has 76 % of carbon and a very big amount of oxygen (24 %). Carbon 1s line fitting, revealed only 42.7 % and 12 % are sp^2 and sp^3 carbon, respectively. 35 % are related to C-OH or C-O-C bonds while the rest are from C=O bonds. O 1s line can even be only fitted to C-O-C bonding indicating that all of the oxygen present is related to hydrocarbons. All these hydrocarbons are related to the immense amount of oxygen present at the surface which most certainly originate from the solvent used for dispersing the graphite.

XPS spectra can be correlated with SEY measurement in which graphite and Graphit 33 also significantly differ (Figure 4.26).

While SEY of graphite is 1.3 and the best achieved result for graphene coatings was $\sim$1, Graphit 33 has a SEY of 2.1. This can be directly compared to bare stainless steel (substrate), which are common in terms of SEY. The spray coating only decreased the

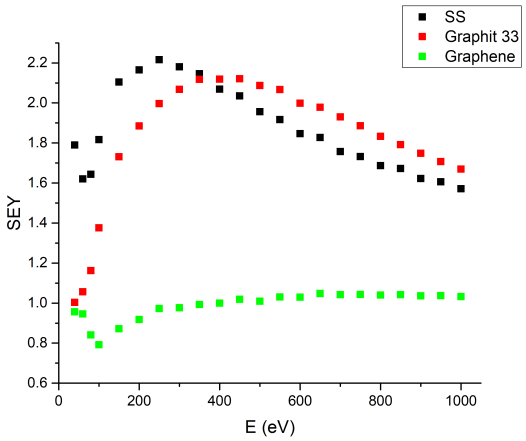

Figure 4.26: SEY curves of bare SS, Graphit 33 and graphene reference sample.

substrate's SEY for only 0.1, when comparing to SS (2.2).

Graphit 33 morphology is slightly different from that of graphite. Looking at SEM images of Graphit 33 (Figure 4.27), structure similarities regarding graphite can be seen. Smaller stacks of graphite (3 to 4 μm) compose the surface, which are significantly smaller than graphite powder, leading to a more uniform surface. Despite the spray coated surface being extremely different from bare stainless steel, it does not influence SEY significantly. This result is a surprise knowing the usual application of such sprays in charged particle optics. It should be however stressed that energy analyzers are used after baking of vacuum systems, which could enhance the desorption of the solvent. It would be, therefore, interesting to test SEY of such surface after baking.

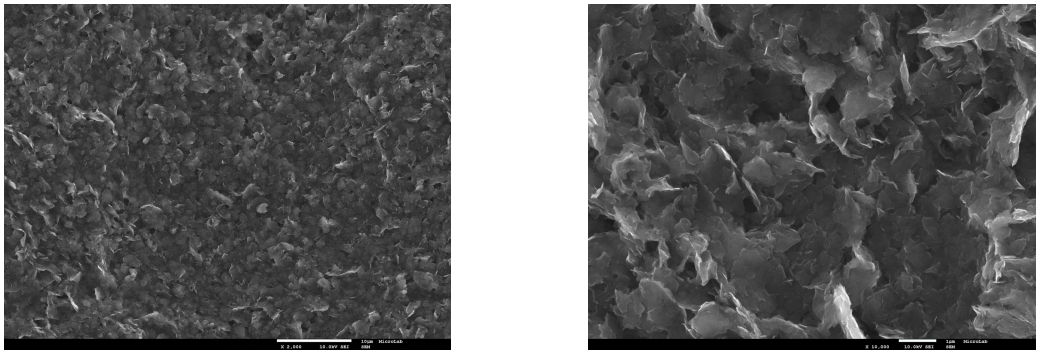

(a) Low magnification (b) High magnification

Figure 4.27: SEM images of Graphit 33 coating.

CHAPTER 5

CONCLUSIONS

The main objective of this Master thesis was to reduce secondary electron emission from technical surfaces by coating them with sp^2 based carbon (graphene).

The study of free standing graphene, acquired from IPFN, was the main focus of this work. Two reference samples were created, one of HOPG and one of graphene, to have in mind the lowest SEY value possible to achieve ($\sim$1) and differences in their curve shape. HOPG was used as a reference for sp^2 based systems regarding C 1s peak in XPS.

In order to coat a metallic surface with this kind of material without affecting its structure and properties, electrophoretic deposition was employed. This technique uses an electrolyte solution, where solid particles are dispersed, and an applied electric field forces the mobility of those particles onto a substrate. From previous studies, isopropanol is commonly used to disperse graphene, whilst hydrochloric acid is suitable for making an electrolyte where graphene is dispersed. For this reason, both were used to make an electrolyte in which graphene was successfully dispersed and deposited. There are a few parameters that influence the efficiency of the technique, so, to optimize the deposition process, different experiments were conducted.

EPD uses two electrodes inside the fluid which drive the electric field. One of those electrodes is used as a substrate, where copper or stainless steel plates were used (common metals used in accelerators chambers and satellites), as for the other one, it was tested gold and stainless steel. A gold counter electrode was found to be the most suitable since graphene structure is preserved and the amount of contaminants are minimal. When using a stainless steel counter electrode, besides the huge amount of contaminants, graphene seemed to be partially transformed into some kind of 3D carbon structures, leaving a minor amount of sp^2 carbon on the deposit.

Three other parameters were also tested, such as: deposition time, applied potential between electrodes and the amount of HCl in the electrolyte. Higher deposition time resulted in thicker deposits which consequently led to lower SEY. This parameter did not have repercussions on the graphene structure since in XPS, sp^2:sp^3 ratio is roughly maintained. With a deposit of 90 minutes, it was possible to reduce SEY down to the reference value. Concerning the applied voltage between the electrodes, deposition time was fixed and five potential values were chosen (20, 30, 40, 50 and 60 V). For the five different potential values used , it is verified that a 40 V deposition led to the lowest SEY of the five, but was the worst coating regarding the sp^2:sp^3 ratio. Lastly, the amount of HCl was studied. Increasing the amount of HCl in the solution resulted in a more conductive medium, but consequently, the gold counter electrodes etching rate also increased. This led to the formation of gold structures in the deposit which increased the SEY of the coating. For this reason, the last two parameters were carefully chosen.

At last, three different coatings were able to achieve SEY of $\sim$1. Two produced coatings with different substrate materials (copper and stainless steel) using a gold counter electrode were directly compared. These two had an identical surface composition ($\sim$95 % of carbon) and a similar sp^2:sp^3 ratio. The main difference between them was in the deposition time. Using a copper substrate, it was possible to achieve the same SEY results as the stainless steel substrate, but in 1/3 of the time. It seems that copper works as a catalyst which facilitates the process of deposition. A third sample was produced using a copper substrate and a stainless steel counter electrode. As already previously claimed, the deposit was full of metallic and organic contaminants, graphene structure was severely damaged and its partial transformation into 3D carbon structures was observed. Despite the strange composition and morphology, it was still possible to reduce its SEY down to the same value of the other coatings. It was also proven that SEY of these graphene coatings increased by $\sim$0.1 after approximately 1 month to air exposure, while baking did not affect it.

Finally, three alternatives to reduce the SEY of a technical surface were tested. Firstly, CVD grown graphene was analyzed and measured. Although some reduction of SEY was observed in one of the samples coated in INL, their structure and composition is far from that of graphene. It could be only concluded that the applied deposition technique is not reliable in producing graphene layers.

Secondly, an EPD was performed using graphite powder instead of graphene. The graphite coating seemed to have slightly higher organic contaminants than the a graphene sample produced with the same parameters, on the other hand, it had a better sp^2:sp^3 ratio. Despite graphene coatings led to lower SEYs, this graphite deposit was still able to reduce SEY of stainless steel from $\sim$2.2 to 1.3, the value typical for bulk graphite.

Finally, a graphite based spray, commonly used to coat electrodes of energy analyzers, was acquired. It was dried exposing it to air and then analyzed. It was observed a significant amount of oxygen in its composition leading to a big contribution of hydrocarbons in

its surface. This might be the reason why its SEY is similar to bare stainless steel. In future studies, baking the deposit might eliminate a major part of these contaminants and maybe reduce its SEY.

Regarding future studies in order to give some continuity to this project, different parameters and some of those already tested, might be studied in more detail. Different electrolyte solutions as well as different electrodes' materials are also worth being investigated. At last, it would be interesting to study the created 3D carbon structures when using stainless steel as counter electrode, and why its SEY is comparable to that of the clean graphene structures.

BIBLIOGRAPHY

[1] R. Salemme, V. Baglin, G. Bregliozzi, P. Chiggiato, and R. Kersevan. "Amorphous Carbon Coatings at Cryogenic Temperatures with LHC Type Beams: First Results with the Coldex Experiment". In: *Proceedings of 6th IPAC, Richmond, USA* (2015), pp. 3112–3114.

[2] A. Santos, N. Bundaleski, B. J. Shaw, A. G. Silva, and O. M. Teodoro. "Increase of secondary electron yield of amorphous carbon coatings under high vacuum conditions". In: *Vacuum* 98 (2013), pp. 37–40.

[3] T. Sian, Y. Lin, R. Valizadeh, O. B. Malyshev, G. Xia, C. Valles, G. Yu, and I. Kinloch. "Graphene coating for the Reduction of the Secondary Electron Yield". In: *Proceedings of 7th IPAC, Busan, Korea* (2016), pp. 3688–3690.

[4] B. J. Á. Shaw. "Projecto e Construção de um Aparelho para a Medição da Taxa de Emissão de Electrões Secundários." In: *Dissertação de Mestrado, Faculdade de Ciências e Tecnologia - Universidade Nova de Lisboa* (2010).

[5] G. Rumolo, F. Ruggiero, and F. Zimmermann. "Simulation of the electron-cloud build up and its consequences on heat load, beam stability, and diagnostics". In: *Physical Review Special Topics - Accelerators and Beams* 4 (2001), pp. 25–36.

[6] I. Montero, L. Aguilera, M. E. Dávila, V. C. Nistor, L. A. González, L. Galán, D. Raboso, and R Ferritto. "Applied Surface Science Secondary electron emission under electron bombardment from graphene nanoplatelets". In: *Applied Surface Science* 291 (2014), pp. 74–77.

[7] V. Baglin, J. Bojko, O. Gröbner, B. Henrist, N. Hilleret, C. Scheuerlein, and M. Taborelli. "The Secondary Electron Yield of Technical Materials and Its Variation With Surface Treatments". In: *Proceedings of 7th EPAC, Vienna, Austria* (2000), pp. 217–221.

[8] N. Bundaleski, B. J. Shaw, A. G. Silva, A. M. C. Moutinho, and O. M.N. D. Teodoro. "Novel Approach to the Semi-Empirical Universal Theory for Secondary Electron Yield". In: *Scanning* 33 (2011), pp. 266–269.

[9] P. Hef, H. C. Hseuh, R. Todd, B. Henrist, N. Hilleret, F. L. Pimpec, R. E. Kirby, M. Pivi, S. Kato, and M. Nishiwaki. "Secondary Electron Emission Measurements for TiN Coating on the Stainless Steel of SNS Accumulator Ring Vacuum Chamber". In: *Proceedings of 9th EPAC, Lucerne, Switzerland* (2004), pp. 5–8.

[10] E. L. Garwin, F. K. King, R. E. Kirby, and O. Aita. "Surface properties of metal-nitride and metal-carbide films deposited on Nb for radio-frequency superconductivity". In: *Journal of Applied Physics* 61 (1987), pp. 1145–1154.

[11] C. Y. Vallgren, S Calatroni, P. C. Pinto, A Kuzucan, H Neupert, and M Taborelli. "Characterization of Carbon Coatings with Low Secondary Electron Yield". In: *Proceedings of 2nd IPAC, San Sebastián, Spain* (2011).

[12] G. Xie, W. Cui, and J. Yang. "A general route towards secondary electron yield suppression based on graphene". In: *Proceedings of 17th ANTEM, Montreal, Canada* (2016), pp. 10–12.

[13] M. Pivi, F. K. King, R. E. Kirby, T. O. Raubenheimer, G. Stupakov, and F. Le Pimpec. "Sharp reduction of the secondary electron emission yield from grooved surfaces". In: *Journal of Applied Physics* 104 (2008), pp. 1–10.

[14] P. Kumar, C. Watts, T. Svimonishvili, M. Gilmore, and E. Schamiloglu. "The Dose Effect in Secondary Electron Emission". In: *IEEE Transactions on Plasma Science* 37 (2009), pp. 1537–1551.

[15] Y. Lin and D. C. Joy. "A new examination of secondary electron yield data". In: *Surf. Interface Anal.* 37 (2005), pp. 895–900.

[16] S. X. Tao, H. W. Chan, and H. van der Graaf. "Secondary Electron Emission Materials for Transmission Dynodes in Novel Photomultipliers: A Review". In: *Materials* 9 (2016) 1017 ().

[17] *Graphene online store - Article, Accessed: 28-07-2018*. URL: \url{https://www.graphenea.com/pages/graphene#.W6QSfdNKi00}.

[18] *sp3 hybridization, Accessed: 03-08-2018*. URL: https://chemistryonline.guru/hybridization-sp3/.

[19] *Hybridization of Atomic Orbitals, Accessed: 03-08-2018*. URL: http://butane.chem.uiuc.edu/cyerkes/Chem102AEFa07/Lecture_Notes_102/Lecture%2015%27-102.htm.

[20] A. Tiwari, P. C. Banerjee, and M. Majumder. "CVD Graphene on Metals for Remarkable Corrosion Resistance". In: *Proceedings of Corrosion and Prevention, Melbourne, Australia* 113 (2012).

[21] N. Bundaleska, D. Tsyganov, A. Dias, and E. Felizardo. "Microwave plasma enabled synthesis of free standing carbon nanostructures at atmospheric pressure conditions". In: *Physical Chemistry Chemical Physics* 20 (2018), pp. 13810–13824.

[22] E. Tatarova, A. Dias, J. Henriques, M. Abrashev, N. Bundaleska, and E. Kovacevic. "Towards large-scale in free- standing graphene and N-graphene sheets". In: *Scientific Reports* 7 (2017) 10175 ().

[23] *Electrophoretic Deposition (EPD), Accessed: 07-08-2018*. URL: https://www.mtm.kuleuven.be/Onderzoek/Ceramics/old-info/EPD.

[24] L. Besra and M. Liu. "A review on fundamentals and applications of electrophoretic deposition (EPD)". In: *Progress in Materials Science* 52 (2007), pp. 1–61.

[25] *Zeta Potential, Accessed: 07-08-2018*. URL: https://en.wikipedia.org/wiki/Zeta_potential.

[26] J. J., V. Tassel, and C. A. Randall. "Mechanisms of Electrophoretic Deposition". In: *Key Engineering Materials* 314 (2006), pp. 167–174.

[27] B. Ferrari and R. Monero. "The conductivity of aqueous Al2O3 slips for electrophoretic deposition". In: *Materials Letters* 28 (1996), pp. 353–355.

[28] J. Binner. *Advanced Ceramic Processing and Technology*. First. Vol. 01. Noyes Publications, 1990.

[29] R. N. Basu, C. A. Randall, and M. J. Mayo. "Fabrication of Dense Zirconia Electrolyte Films for Tubular Solid Oxide Fuel Cells by Electrophoretic Deposition". In: *Journal of the American Ceramic Society* 84 (2001), pp. 33–40.

[30] *Casa XPS - Help Manual - XPS Information - XPS Instrumentation, Accessed: 30-07-2018*. URL: \url{http://www.casaxps.com/help_manual/XPSInformation/XPSInstr.htm}.

[31] C. D. Wagner, L. E. Davis, M. V. Zeller, J. A. Taylor, R. H. Raymond, and L. H. Gale. "Empirical Atomic Sensitivity Factors for Quantitative Analysis by Electron Spectroscopy for Chemical Analysis". In: *Surface and Interface Analysis* 3 (1981), pp. 211–225.

[32] *Casa XPS - Help Manual - XPS spectra, Accessed: 04-08-2018*. URL: \url{http://www.casaxps.com/help_manual/manual_updates/xps_spectra.pdf}.

[33] *XPS Reference pages - Modified Auger Parameter, Accessed: 10-08-2018*. URL: \url{http://www.xpsfitting.com/2008/09/modified-auger-parameter-defined.html}.

[34] *XPS Reference pages - Shake-up satellites, Accessed: 13-08-2018*. URL: http://www.xpsfitting.com/2012/08/shake-up-structure.html.

[35] *XPS Reference pages - Multiplet Splitting, Accessed: 13-08-2018*. URL: http://www.xpsfitting.com/2008/09/multiplet-splitting.html.

[36] *XPS Casa - Help Manual - Line Shapes, Accessed: 20-08-2018*. URL: http://www.casaxps.com/help_manual/line_shapes.htm.

[37] *Scanning Electron Microscopy - Electron Emission Mechanisms, Accessed: 28-08-2018*. URL: https://en.wikipedia.org/wiki/Scanning_electron_microscope.

[38] *Scanning Electron Microscopy - Instrumentation, Accessed: 28-08-2018*. URL: https://www.nanoscience.com/techniques/scanning-electron-microscopy/.

[39] A. O. Neill, U. Khan, P. N. Nirmalraj, J. Boland, and J. N. Coleman. "Graphene Dispersion and Exfoliation in Low Boiling Point Solvents". In: *The Journal of Physical Chemistry* 115 (2011), pp. 5422–5428.

[40] A. Dias, N. Bundaleski, E. Tatarova, F. M. Dias, M. Abrashev, U. Cvelbar, O. M.N. D. Teodoro, and J. Henriques. "Production of N-graphene by microwave N_2-Ar plasma". In: *Journal of Physics D: Applied Physics* 49 (2016) 055307 ().

[41] G. B. D. Briggs. *High Resolution XPS of Organic Polymers: The Scienta ESCA300 Database*. 1st ed. Wiley, 1992.

[42] G. Paolicelli, S. Ferrer, and F. Comin. "Separation of the sp 3 and sp 2 components in the C 1 s photoemission spectra of amorphous carbon films". In: *Physical Review B* 54 (1996), pp. 8064–8069.

[43] *XPS Reference Pages - Carbon, Accessed: 25-08-2018*. URL: http://www.xpsfitting.com/search/label/carbon.

[44] *XPS Reference Pages - Oxygen, Accessed: 25-08-2018*. URL: http://www.xpsfitting.com/search/label/Oxygen.

[45] Z. Insepov, V. Ivanov, and H. Frisch. "Comparison of Candidate Secondary Electron Emission Materials". In: *UChicago Argonne, LLC - Argonne National Laboratory* ().

[46] M. C. Biesinger, L. W. M. Lau, A. R. Gerson, R. St, and C Smart. "Applied Surface Science Resolving surface chemical states in XPS analysis of first row transition metals , oxides and hydroxides : Sc , Ti , V , Cu and Zn". In: *Applied Surface Science* 257 (2010), pp. 887–898.

[47] M. C. Biesinger and B. P. Payne. "Author ' s personal copy Resolving surface chemical states in XPS analysis of first row transition metals , oxides and hydroxides : Cr , Mn , Fe , Co and Ni". In: *Applied Surface Science* 257 (2010), pp. 2717–2730.

[48] S. Modification, T. Smt, G. Baiocco, M. Simoncini, V. Tagliaferri, and N. Ucciardello. "Combined electrodeposition of copper and graphene nano-platelets on alluminium ' s alloys substrate for corrosion protection". In: *Proceedings of 30th International Conference on Surface Modification Technologies, Milan, Italy* (2016).

[49] C. D. Wagner, W. M. Riggs, L. E. Davis, J. F. Moulder, and G. E. Mullenberg. *Handbook of X-Ray Photoelectron Spectroscopy*. 1st ed. Perkin-Elmer Corporation, Physical Electronics Division, 1979.

[50] G. Beamson and D. Briggs. "High resolution monochromated X-ray photoelectron spectroscopy of organic polymers : A comparison between solid state data for organic polymers and gas phase data for small molecules". In: *Molecular Physics: An International Journal at the Interface Between Chemistry and Physics* 76 (1992), pp. 919–936.